


Summer 2018

Aerothermodynamic Analysis of a Mars Sample Return Earth-Entry Vehicle

Daniel A. Boyd
Old Dominion University

Follow this and additional works at: https://digitalcommons.odu.edu/mae_etds

 Part of the [Aerodynamics and Fluid Mechanics Commons](#), [Space Vehicles Commons](#), and the [Thermodynamics Commons](#)

Recommended Citation

Boyd, Daniel A.. "Aerothermodynamic Analysis of a Mars Sample Return Earth-Entry Vehicle" (2018). Master of Science (MS), thesis, Mechanical & Aerospace Engineering, Old Dominion University, DOI: 10.25777/xhmz-ax21
https://digitalcommons.odu.edu/mae_etds/43

This Thesis is brought to you for free and open access by the Mechanical & Aerospace Engineering at ODU Digital Commons. It has been accepted for inclusion in Mechanical & Aerospace Engineering Theses & Dissertations by an authorized administrator of ODU Digital Commons. For more information, please contact digitalcommons@odu.edu.

**AEROTHERMODYNAMIC ANALYSIS OF A MARS SAMPLE RETURN
EARTH-ENTRY VEHICLE**

by

Daniel A. Boyd
B.S. May 2008, Virginia Military Institute
M.A. August 2015, Webster University

A Thesis Submitted to the Faculty of
Old Dominion University in Partial Fulfillment of the
Requirements for the Degree of

MASTER OF SCIENCE

AEROSPACE ENGINEERING

OLD DOMINION UNIVERSITY
August 2018

Approved by:

Robert L. Ash (Director)

Oktay Baysal (Member)

Jamshid A. Samareh (Member)

Shizhi Qian (Member)

ABSTRACT

AEROTHERMODYNAMIC ANALYSIS OF A MARS SAMPLE RETURN EARTH-ENTRY VEHICLE

Daniel A. Boyd
Old Dominion University, 2018
Director: Dr. Robert L. Ash

Because of the severe quarantine constraints that must be imposed on any returned extraterrestrial samples, the Mars sample return Earth-entry vehicle must remain intact through sample recovery. Vehicles returning on a Mars-Earth trajectory will attain velocities exceeding any that have been experienced by prior space exploration missions, with velocities approaching 14 km/s. Velocities as high as these will encounter significant heating during atmospheric re-entry to Earth.

The purpose of this study has been to systematically investigate the aerothermodynamic challenges that will result from a Mars sample return, Earth-entry vehicle design. The goal was to enable efficient estimation of maximum stagnation point convective and radiative heating that will be encountered during Earth-entry over a wide range of spherically blunted cone angles, entry velocities, flight path angles, and ballistic coefficients.

Assembling a robust and validated aerothermodynamic database for a potential Mars sample return Earth-entry vehicle has been accomplished by estimating peak heating over a wide range of possible designs. This goal was achieved by utilizing fundamental knowledge, along with the use of engineering analysis tools, such as POST2 (Program to Optimize Simulated Trajectories II) and LAURA (Langley Aerothermodynamic Upwind Relaxation Algorithm) computational fluid dynamics analysis.

The aerothermodynamic analysis conducted in this thesis provides a catalog of heating trends to be used for optimal selection of mission design constraints such as vehicle geometry, thermal protection system, and entry trajectory, with the primary goal of returning a Mars soil and atmospheric sample for thorough analysis on Earth; this acts as a step towards safely landing humans on the Martian surface.

Copyright, 2018, by Daniel Angelo Boyd, All Rights Reserved

This thesis work is dedicated to my Parents, and to my Love.

Mom, Dad – Throughout my entire life, you have always believed in me and pushed me to follow my heart and my dreams. I would not be the man that I am today without your love, patience, encouragement, and when needed...a swift kick the rear! I love you more than you can ever know, and I want to thank you for everything you have done for me.

Michelle – My love, you are the source of my inspiration and my motivation. You make me believe in myself at times when I do not, and I am a better person because of it. I want to thank you for your constant love, support and understanding, without which none of this would have been possible. Hearts and stuff.

ACKNOWLEDGMENTS

This thesis would not have been successfully completed without the vital contribution of many people. My advisor and mentor, Dr. Robert Ash, who has always guided me and challenged me throughout my graduate studies, deserves special recognition. I would like to thank Dr. Jamshid Samareh, my research mentor at NASA Langley for all of his constant support in helping me make sense of the concepts and the research process included in my studies, and especially in my efforts to learn Python coding. Thanks also go to Dr. Shizhi Qian and Dr. Oktay Baysal for serving on my thesis committee, and for hours of instruction in and out of the classroom, without which I would not have been able to understand the complexity of my studies. I extend many thanks as well to Dr. Tom West, the resident LAURA expert at the Vehicle Analysis Branch, for answering the many, many questions I had in learning to run the code.

TABLE OF CONTENTS

	Page
LIST OF TABLES	ix
LIST OF FIGURES	x
Chapter	
1. INTRODUCTION	1
1.1. THEORETICAL FORMULATIONS.....	2
1.1.1. ENTRY VEHICLE SHAPES	3
1.1.2. HYPERSONIC FLOW CHARACTERISTICS OF BLUNT-NOSED GEOMETRIES	5
1.1.3. SHOCK LAYER GAS PHYSICS	6
1.2. PURPOSE.....	9
1.3. PROBLEM.....	10
2. TOOLS AND SOFTWARE EMPLOYED IN RESEARCH	12
2.1. POST2.....	12
2.1.1. CONVECTIVE AND RADIATIVE HEATING ESTIMATES.....	12
2.2. LAURA CFD.....	14
2.3. M-SAPE.....	16
3. METHODOLOGY AND PROCEDURE.....	18
3.1. BASELINE MODEL.....	18
3.2. POST2 ANALYSIS.....	19
3.3. LAURA ANALYSIS.....	20
4. RESULTS	21
4.1. TRAJECTORY RESULTS.....	21
4.2. LAURA CFD RESULTS.....	26

4.3 SURROGATE MODEL DEVELOPMENT	35
5. CONCLUSIONS AND FUTURE WORK	42
REFERENCES	44
APPENDICES	49
A. TABLE OF LAURA RESULTS	49
VITA.....	52

LIST OF TABLES

Table	Page
1. Sample Return Capsule (SRC)/Small Entry Probe Earth Entry Vehicle Characteristics	19
2. Representation of POST2 results.....	21
3. Parameters required to initiate baseline LAURA runs, along with specified initial conditions (relative velocity, atmospheric density and temperature)	27
4. Representation of a LAURA/HARA result	29
5. Error of Surrogate Models for Convective and Radiative Heat Flux	39

LIST OF FIGURES

Figure	Page
1. Shadowgraph images showing shock wave flow characteristics for nose geometries	2
2. Representations of low drag (a) and high drag (b) blunted atmospheric entry vehicles. These are characteristic of the extremes of the spectrum of entry vehicle shapes	3
3. Two-dimensional geometries of a sphere-cone (left) and a spherical body (right)	4
4. Shock shapes for flow past a sphere for various Mach numbers	5
5. Plot of change in shock standoff distance vs. value of specific heat, γ	8
6. Plot of air species concentrations vs. free stream velocity	8
7. 7. M-SAPE Flow Chart	17
8. POST2 results showing case-by-case relative velocity for maximum heating	22
9. Approximate maximum convective heat flux, correlated with flight path angle (FPA), and entry velocity (V_e) for various combinations of cone angle and ballistic coefficient (BC)	24
10. Approximate maximum convective heat flux loads correlated with flight path angle (FPA), and entry velocity (V_e) for different cone angles and ballistic coefficients (BC)	25
11. Non-converged LAURA solution for convective heat flux (q_w) vs. the grid x-axis	28
12. Converged LAURA solution for convective heat flux, $q_{conv}(x)$ vs. the grid location on the x-axis	28
13. Atmospheric Density and Relative Velocity at maximum total heating for all LAURA/HARA runs. Blue dots represent converged solutions, while red dots represent non-converged solutions	29
14. LAURA/HARA Results for 45 Degree Cone Angle, correlating Atmospheric Density with Relative Velocity for Maximum Stagnation Heating	31
15. LAURA/HARA Results for 50 Degree Cone Angle, correlating Atmospheric Density with Relative Velocity for Maximum Stagnation Heating	32
16. LAURA/HARA Results for 55 Degree Cone Angle, correlating Atmospheric Density with Relative Velocity for Maximum Stagnation Heating	33

17. LAURA/HARA Results for 60 Degree Cone Angle, correlating Atmospheric Density with Relative Velocity for Maximum Stagnation Heating	34
18. Comparison of Actual Convective Heat Flux (LAURA results) vs. Approximate Convective Heat Flux (Surrogate Model).....	37
19. Comparison of Actual Radiative Heat Flux (LAURA results) vs. Approximate Radiative Heat Flux (Surrogate Model).....	38
20. Maximum Stagnation Point Convective Heat Flux Surrogate model based on LAURA results	40
21. Maximum Stagnation Point Radiative Heat Flux Surrogate model based on LAURA results	41

CHAPTER 1

INTRODUCTION

Germany first launched its “Vergeltungswaffe Eins” or “Vengeance Weapon No. 1” during its counter attack on England in June 1944. The subsequent launching of the V-2 Rockets in September, during a strike on London, was significant because these rockets reached supersonic speeds of up to Mach 5.¹ Long-range missiles and rockets were only feasible if their trajectories reached high altitudes above the Earth’s surface, in order to minimize drag resulting from their excessive speeds. As the velocities and the range of these ballistic missiles began to increase, the characteristics of the aerodynamic flow changed as well. Researchers discovered that, along with stabilization and aerodynamic loads, aerodynamic heating became an issue at hypersonic speeds (above Mach 5).¹ New designs for rocket and missile nose geometries allowed the first intercontinental ballistic missiles (ICBMs) to re-enter the Earth’s atmosphere at these very high velocities without breaking apart. History shows that these technologies became research focal points in the 1950s and 1960s, when space flight became feasible. Getting into space may have been a major technological challenge, but returning an intact payload to the surface of the Earth from orbit was just as important. At hypersonic speeds, many more factors play an integral role when attempting to characterize and accommodate these re-entry flows. Spacecraft forebody geometry and shock layer gas physics, as well as convective and radiative heating are all major system design challenges.

1.1 Theoretical Formulations

In 1951, National Advisory Committee for Aeronautics (NACA) engineers, H. Julian Allen and A. J. Eggers, Jr. determined that a blunt body was the optimal shape for a re-entry vehicle thermal protection system, due to its high drag and large surface areas.² Allen and Eggers were able to demonstrate that the heat load produced by an atmospheric entry vehicle was inversely proportional to the drag coefficient.¹ The higher drag of a blunt body results in a more rapid deceleration, as well as reduced local heating levels, on the entry vehicle surfaces. Moving through the Earth's atmosphere at hypersonic velocities, the blunt body shape of a re-entry vehicle causes the air to act as a cushion, pushing the shockwave and the heated shock layer away from the vehicle.³ Various concepts were evaluated using shadowgraph flow visualization, as depicted in Figure 1. Earlier pointed-nose concepts (*INITIAL CONCEPT* in Figure 1) proved

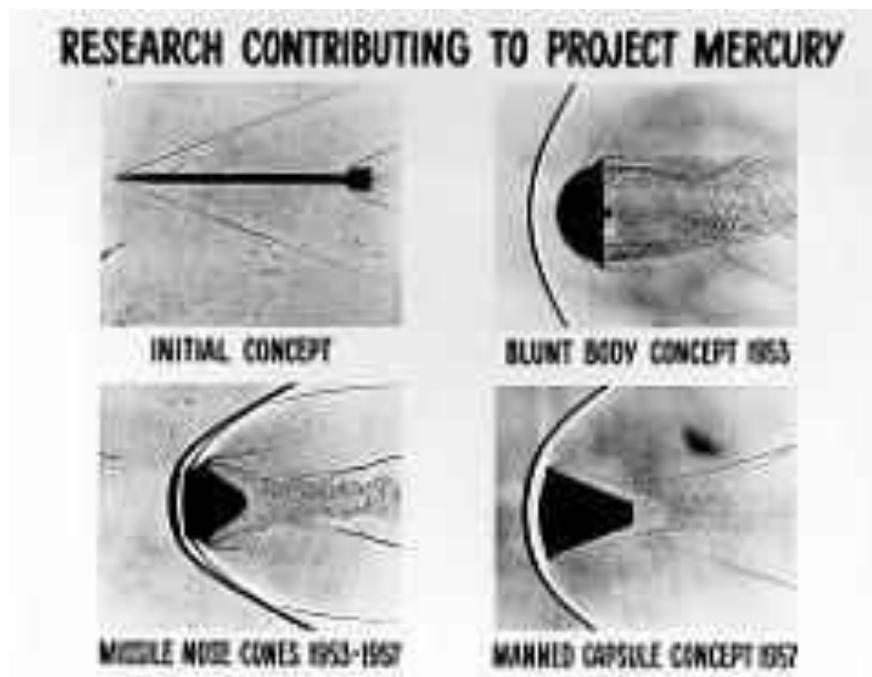


Fig. 1. Shadowgraph images showing shock wave flow characteristics for nose geometries.⁴

to be inadequate, since their narrow sharp tips did not allow for the shock wave to move away from the body, which caused the nose to overheat and break apart. Referring to the Figure 1, detached shock waves can be seen forward of the blunt body geometries.⁴

1.1.1 Entry Vehicle Shapes

Most contemporary ballistic entry vehicle geometries incorporated either a low drag forebody or a high drag forebody, as illustrated schematically in Figure 2. For similar characteristic entry trajectories, the low drag forebody decelerates at a lower altitude than the high drag forebody, meaning that the low drag geometry will experience higher velocities while traversing the more-dense portion of the atmosphere, leading to higher levels of heat flux.³ Because of this reason, blunt forebody designs have been employed for atmospheric re-entry of space probes.

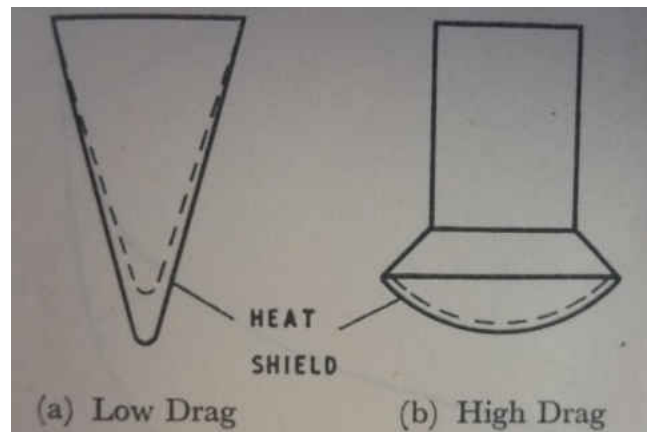


Fig. 2. Representations of low drag (a) and high drag (b) blunted atmospheric entry vehicles.

These are characteristic of the extremes of the spectrum of entry vehicle shapes.³

The two most commonly used geometries are the sphere-cone and the spherical body, as depicted in Figure 3.⁵ The sphere-cone generally consists of a spherical nose and a shortened cone (frustum) blended along the tangent line between the nose cone and shoulder radius. The spherical body consists of a spherical “dish” type section blended with the shoulder radius. Nose

radius, R_n , cone angle, θ_c , shoulder radius, R_s , and base radius, R_b all are design variables. Smaller nose radii and smaller half angles, like those in the low drag designs, tend to lead to greater aerodynamic heating due to the reduced bluntness, as well as the more-shallow shockwave region forward of the spacecraft body.⁶

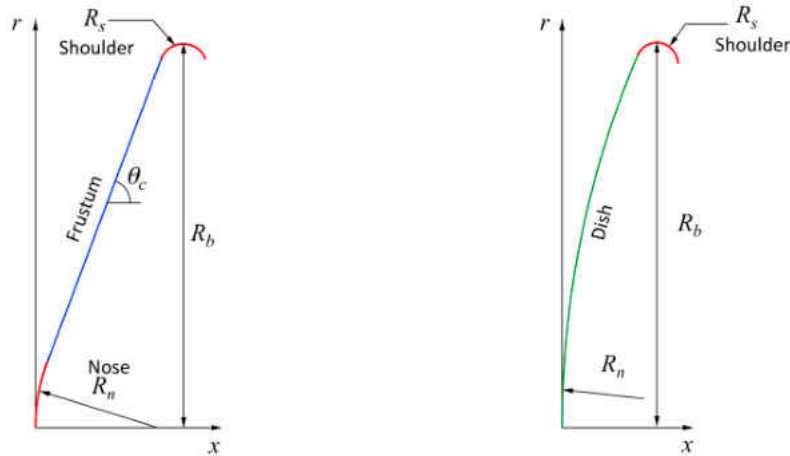


Fig. 3. Two-dimensional geometries of a sphere-cone (left) and a spherical body (right).⁵

From a ballistic trajectory standpoint, assuming that the entry angle-of-attack is zero, higher cone half-angles cause the shape of the aero shell to be more blunt, leading to higher drag coefficients.⁶ This results in the spacecraft experiencing slightly lower levels of heating, while causing it to decelerate more rapidly.¹ When considering blunted entry vehicles at zero angles-of-attack (ballistic entry), maximum heating occurs at the nose, termed the *stagnation point*, specifically for smaller vehicles with shorter running lengths. By altering the entry vehicle angle-of-attack, aerodynamic heating is reduced and the vehicle generates lift to adjust its trajectory. However, for the purposes of determining maximum heat flux at the stagnation point, only ballistic trajectories are investigated in this study.

1.1.2 Hypersonic Flow Characteristics of Blunt- Nosed Geometries

The main difference between subsonic and supersonic flight is the presence of a shock layer, and in blunt body cases, the shock front is detached from the body. In cases where the Mach number is greater than 5, the shock layer shape around the body causes significant changes in standoff distances and associated pressure gradients.³ As the Mach number increases, local shock standoff distances decrease.³ This causes the shock layer thickness to decrease, and the resulting pressure gradient forces experienced within the shock layer increase, acting against the entry vehicle body, as shown in Figure 4. The pressure within the shock layer falls from extreme high

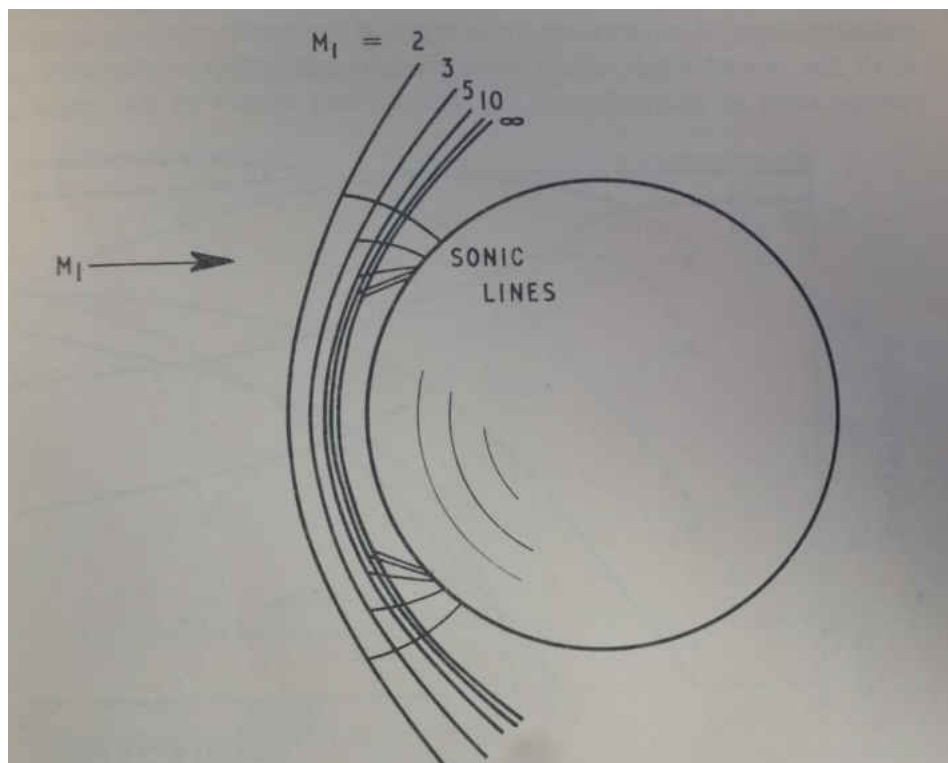


Fig. 4. Shock shapes for flow past a sphere for various Mach numbers.³

pressure values near the stagnation point to levels much closer to the free stream pressures in areas farther away from the stagnation point.³ Because of this, pressure gradients experienced on

the aft body during hypersonic flow decay more rapidly.⁷ This results in lower pressures near the aft end of the entry vehicle, meaning that the primary aerodynamic drag forces act on the forebody.

1.1.3 Shock Layer Gas Physics

Hypersonic flows can be modeled utilizing either macroscopic (continuum) or microscopic (molecular) scales, and when the gradients of the macroscopic variables become steep enough that their scale lengths are the same order as the average distance travelled by molecules between collisions, i.e. the mean free path, the transport terms in the Navier-Stokes equations of continuum gas dynamics fail.⁸ Therefore, flow in rarefied and low density gas environments needs to be examined at the molecular level.

For many aerodynamic applications, especially in subsonic flight, the perfect gas model can be utilized for designing aircraft. The perfect gas model assumes that the atoms and molecules making up the flow field are chemically inert.⁹ However, for higher velocities and the resulting shock layer, non-equilibrium species models are required. At hypersonic speeds, local atmospheric molecules that enter shockwave regions become superheated by compression and cause a number of reactions. First, dissociation and ionization of gas occur, due to extremely high temperatures within the high levels of deceleration by shockwaves.¹⁰ And second, there is diffusion of atoms and ions, which also have the chance to recombine with a high specific energy release.¹⁰ Non-equilibrium real gas models take these reactions into account, but the time interval during which these atmospheric particles enter the shock layer, become activated, and depart, is extremely short.³ Therefore, not all chemical reactions are complete before the reacting molecules exit the shock layer, which makes it extremely difficult to replicate and measure these “truncated” chemical reactions with a mathematical model. However, the extreme temperatures

that characterize the shock layer atoms and molecules tend to be overlooked because of the transient effects, enabling somewhat simplistic approximations. As a result, the specific heat ratio, γ , behind these shock waves can change significantly; as the velocity increases in the flowfield, the value of γ decreases.³ This has a significant effect on the flowfield, and, as depicted in Figure 5, the specific heat ratio decreases, as does the shock standoff distance.^{3,11} This high temperature gas layer produces significant local levels of gaseous radiation. This occurs because of the immense energy released from the very large number of chemical reactions that occur within the shock layer, through the processes of dissociation and ionization, along with recombination. These reactions require very short, but finite, amounts of time to achieve their local equilibrium concentrations. Such characteristic times, before equilibrium is achieved, are called the *relaxation times*. Even at high hypersonic speeds, these processes may not have sufficient residence times to reach equilibrium within the shock layer.^{3,10,12} This is why non-equilibrium real gas effects within the stagnation region of the shock layer must be considered. Less intricate flows, such as those at supersonic and lower hypersonic Mach numbers, can use fewer species, because the primary molecules making up the local atmosphere only begin to dissociate when the stagnation conditions behind the shock layer exceed the temperature and pressure levels associated with different freestream velocity levels.³ Figure 6 shows the mole fraction concentrations of the primary atmospheric molecules as velocity increases. Therefore,

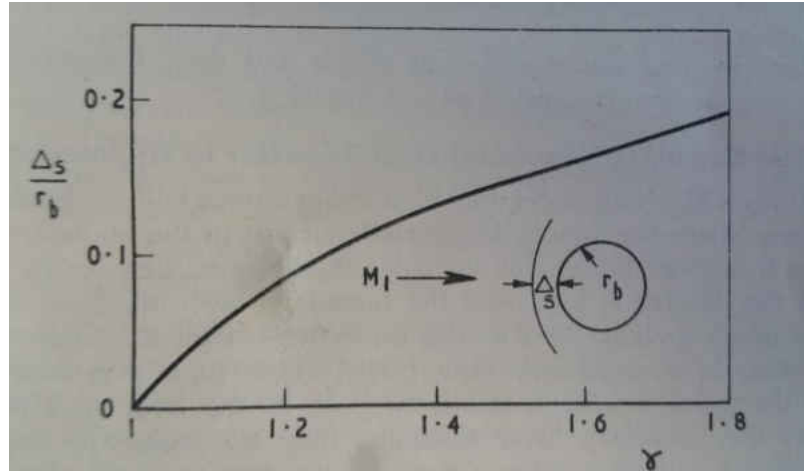


Fig. 5. Plot of change in shock standoff distance vs. value of specific heat, γ .³

more accurate models for higher hypersonic velocities require a more robust species model. This requires the use of a two temperature, multi-species atmospheric model, specifically for high Mach number flows, an eleven species model. The two temperatures for the model represent an

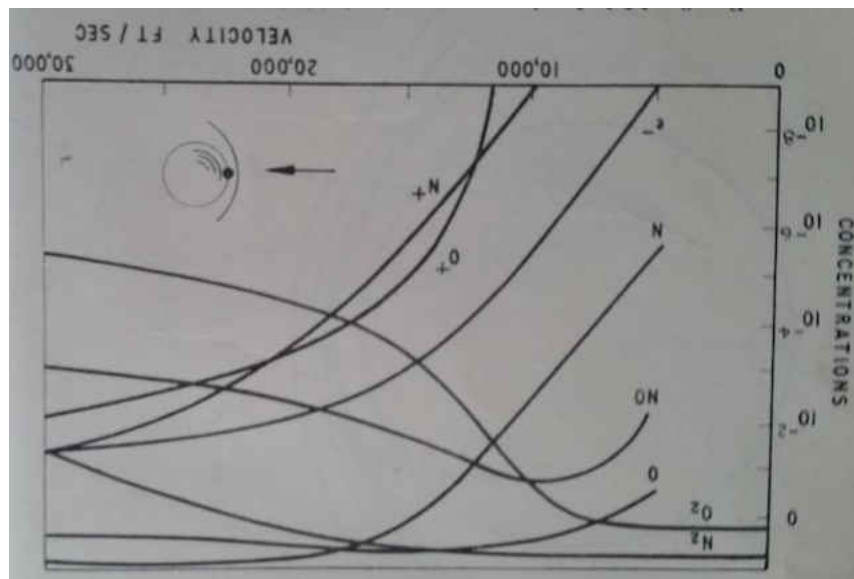


Fig. 6. Plot of air species concentrations vs. free stream velocity.³

approximation of realistic multi-temperatures that occur in complex molecular and atomic mixtures, and the translational temperature of the heavy particles, such as molecules and atoms,

as well as the rotational temperature of molecules.¹² The first temperature is assumed to characterize heavy particle translational and molecular rotational energies, while the second temperature approximated by the model describes molecular vibrational, electron translational, and electronic excitation energies, assessed by Park.¹³ For these flow conditions, a robust model incorporating the molecules and atoms that make up that part of the atmosphere is required, as well. The eleven species within the model include N, O, N₂, O₂, NO, N⁺, O⁺, N₂⁺, O₂⁺, NO⁺, and e⁻ with a 21% O₂ and 79% N₂ to approximate the composition of air.^{11,13} All possible chemical reactions associated with these species, including their reverse- reactions, are considered. The two-temperature chemical kinetic model for air is obtained by comparing theoretical results with experimental data from shock tubes and ballistic range experiments, in addition to instrumented flight experiments.

1.2 Purpose

The purpose of this study has been to investigate systematically the aerothermodynamic challenges that will result from a Mars sample return, Earth-entry vehicle design. Because of the severe quarantine constraints that must be imposed on any returned extraterrestrial samples, the Earth-entry vehicle must remain intact through sample recovery. While the recovered sample will likely be some of the most valuable material ever brought to Earth, the goal of this thesis has been to enable efficient estimation of maximum stagnation point convective and radiative heating that will be encountered during Earth entry over a wide range of entry velocities, flight path angles, and ballistic coefficients.

A range of possible Earth-return trajectories originating from Mars has been examined. The resulting Earth return vehicles could possess entry velocities approaching 15 km/s. By

comparison, lunar return missions during the Apollo program had re-entry velocities of approximately 11 km/s, a significant difference.¹⁴⁻¹⁷

1.3 Problem

By the mid-1960s, researchers had gained sufficient understanding of high speed atmospheric Earth entry to enable safe re-entry for Earth escape velocities levels (11 km/s); since lunar return velocities approached 11 km/s for the Apollo missions, that was a logical upper limit at that time.¹⁴⁻¹⁷ Most of the major research efforts related to the aerothermodynamics associated with these extreme entry velocities were discontinued after the Apollo program, and research efforts shifted toward low-Earth orbit return in support of the reusable Space Shuttle re-entry program. Even with advances in technology and theory, the majority of space-related missions encompassed satellite orbit placement and one-way deep space probes, along with missions to other celestial bodies. Missions incorporating recoverable Earth return systems have been characterized mostly by velocities that were below the approximate 11.2 km/s Earth escape velocity.¹⁸ Since the Apollo program, new data enhancing our understanding of molecular gas dynamics and high speed flows are beginning to allow for more-detailed studies that incorporate Mars return systems. The integrity and accuracy of the re-entry vehicle models studied previously require verification related to possible re-entry velocities approaching 15 km/s. Since frictional heat flux has been related to the drag force acting at the entry velocity, local stagnation heat flux 2.5 times greater than the Apollo re-entry rates may be encountered. These types of calculations require accurate estimates in solving complex systems of partial differential equations, which translate to prohibitive computational resource requirements with associated turnaround time bottlenecks. Fortunately, with advances in computer processing power, more accurate calculations are achievable, which is especially important since recreating desired

hypervelocity flow conditions experimentally, employing wind tunnels and shock tubes, is extremely difficult and expensive. Flight test data would obviously provide the most reliable design data, although this, again, is very expensive and time consuming. Numerical simulations allow for faster, more realistic estimates in characterizing these limiting design problems, and enable more precise designs. In this way, the final entry capsule design should simultaneously require smaller mass and volume margins, even as it reduces the risks associated with Earth return.

CHAPTER 2

TOOLS AND SOFTWARE EMPLOYED IN RESEARCH

In order to obtain reliable simulations while conducting the research, a number of software packages were employed. Results from these calculations were compiled into an aerothermodynamic database that is expected to be integrated into the M-SAPE program.

2.1 POST2

The Program to Optimize Simulated Trajectories II (POST2) is a generalized point mass, discrete parameter targeting and optimization program.¹⁹ This package was used to estimate the atmospheric densities and the temperatures, as well as the relative velocity at which peak heating occurred, over a range of input parameters including the entry velocity, ballistic coefficient, flight path angle, and cone angle. POST2 could target and optimize point mass trajectories for multiple powered or unpowered vehicles near an arbitrary rotating, oblate planet. Other projects that have used POST2 include the Mars Exploration Rover (for its entry, descent, and landing on Mars), the *Stardust*, *Genesis*, and *Huygens* Entry Probes, and many others.²⁰ The program utilizes a 4th order Runge-Kutta numerical integration method for trajectory simulations, incorporating the 1976 U.S. Standard Atmosphere model. POST2 allows for both three degrees of freedom (3-DOF) and six degrees of freedom (6-DOF) trajectory calculations. Approximate aerothermodynamic behavior related to convective and radiative heat flux estimates utilized the Sutton and Graves model and Tauber-Sutton model, respectively.

2.1.1 Convective and Radiative Heating Estimates

Fay-Riddell theory¹⁰ and the Sutton and Graves model²¹ correlate stagnation point heating with freestream density and velocity, where that heat flux is represented:

$$\dot{q}_{conv} = C\rho^N V^M \quad \left[\frac{W}{m^2}\right] \quad (1)$$

The correlation coefficient, C_{conv} , is defined:

$$C_{conv} = (1.83 \times 10^{-8})(R_n)^{-1/2}(1-g_w), \quad (2)$$

where R_n is the nose radius and g_w represents the ratio of wall enthalpy (h_w) to total enthalpy (h_0).^{21,22} Here, the ratio of wall enthalpy to total enthalpy is extremely small, i.e. $g_w \ll 1$ because, for re-entry, the local enthalpy of the atmosphere is much smaller than the enthalpy of the entry vehicle due to these extremely high entry velocities. Therefore, g_w effects were neglected.^{22,23}

Under those conditions, the two equations can be combined to yield:

$$\dot{q}_{conv} = k \sqrt{\frac{\rho}{R_n}} V^3. \quad \left[\frac{W}{m^2}\right] \quad (3)$$

For Sutton-Graves, the constant, k , is based on the specific planetary atmospheric composition.^{22,23}

As stated before, at super orbital speeds, bi-directional radiative heat transfer becomes much more significant. The Tauber and Sutton model²⁴ is commonly employed to estimate the radiative stagnation point heat flux contribution, i.e.

$$\dot{q}_{rad} = C_{rad} R_n^a \rho^b f(V) \quad \left[\frac{W}{m^2}\right]. \quad (4)$$

Here, C_{rad} is a constant based on planetary atmospheric conditions, and $f(V)$ is a function of velocity and was tabulated in Tauber and Sutton.²⁴ Consequently, total stagnation point heating could be estimated combined convective and radiative heating estimates from Eqs. (3) and (4) to yield:

$$\dot{q}_{total} = \dot{q}_{conv} + \dot{q}_{rad} \quad (5)$$

2.2 LAURA CFD

The Langley Aerothermodynamic Upwind Relaxation Algorithm (LAURA) is a special-purpose CFD tool for hypersonic re-entry physics and chemistry. The LAURA code is a structured, multi-block, computational aerothermodynamic simulation code, and it shares gas physics modules, MPI modules, and some fundamental data set modules with the unstructured-grid code FUN3D.²⁵ LAURA utilizes thin layer formulations for the Navier-Stokes equations, coupled with user-specified reacting species equations based on atmospheric composition. For this thesis research, the flow field has been assumed to be in chemical and thermal non-equilibrium, utilizing 11 reacting species, with a two-temperature model. Radiation equilibrium at the wall has been assumed in calculations for the wall temperature, and an emissivity of 0.89 has been assumed.

LAURA solves the Navier-Stokes system of equations, formulated to solve simultaneously the continuity equation, the momentum equations, and energy equations. Utilizing the procedure developed by Gnoffo²⁶, the Navier-Stokes equations were represented in integral forms for the conservation laws, and are applied to individual *control volume* cells in the computational domain, written as:

$$\iiint \frac{\partial \mathbf{Q}}{\partial t} d\Omega + \iint \mathbf{F} \cdot \mathbf{n} d\sigma = \iiint \dot{\omega} d\Omega \quad (6)$$

where the first integral describes the time rate of change of conserved quantities, \mathbf{Q} , in the control volume. The second integral describes convective and dissipative flux, \mathbf{F} , through the cell walls, and the third integral accounts for sources or sinks of conserved quantities within the control volume.³⁹ The geometric quantities Ω , σ , and \mathbf{n} define the cell volume, the cell wall area, and the outward-drawn unit normal vector, respectively.²⁷ The inviscid, viscous, and source terms for the complete conservation laws were represented:

$$\mathbf{F} \cdot \mathbf{n} = \mathbf{G} + \mathbf{H} \quad (7)$$

where \mathbf{G} defines the inviscid terms and \mathbf{H} defines the viscous terms.²⁶ The modeled system includes species continuity equations, three momentum equations, and three energy equations describing conservation of vibrational, electronic, and total energies. For high hypersonic flow fields, reacting gas, thermal non-equilibrium two-temperature approximation²⁸ models must be taken into account, and the vectors \mathbf{G} , \mathbf{H} , and $\dot{\boldsymbol{\omega}}$ are defined:

$$\mathbf{Q} = \begin{bmatrix} \rho_s \\ \rho u \\ \rho v \\ \rho w \\ \rho E \\ \rho e_V \end{bmatrix} \quad (8)$$

$$\mathbf{G} = \begin{bmatrix} \rho_s U \\ \rho U u + p n_x \\ \rho U v + p n_y \\ \rho U w + p n_z \\ \rho U h \\ \rho U e_V \end{bmatrix} \quad (9)$$

$$\mathbf{H} = \begin{bmatrix} -\rho D_s \frac{\partial y_s}{\partial s_n} \\ -\tau_{nx} \\ -\tau_{ny} \\ -\tau_{nz} \\ -u\tau_{nx} - v\tau_{ny} - w\tau_{nz} - \eta \frac{\partial T}{\partial s_n} - \eta_V \frac{\partial T_V}{\partial s_n} - \rho \sum_{s=1}^{11} h_s D_s \frac{\partial y_s}{\partial s_n} \\ -\eta_V \frac{\partial T_V}{\partial s_n} - \rho \sum_{s=1}^{11} h_{V,s} D_s \frac{\partial y_s}{\partial s_n} \end{bmatrix} \quad (10)$$

$$\dot{\boldsymbol{\omega}} = \begin{bmatrix} \dot{w}_s \\ 0 \\ 0 \\ 0 \\ q_{rad} \\ \dot{w}_V \end{bmatrix} \quad (11)$$

The first element of the vectors defined in Equations (8) thru (11) controls species conservation; the next three elements impose the x -, y -, and z -components of the conservation of momentum equations; the fifth element maintains total energy conservation, and finally the sixth element maintains vibrational/electronic energy conservation.²⁶

2.3 M-SAPE

The Multi-Mission System Analysis for Planetary Entry (M-SAPE) is a system analysis tool developed for use by planetary probe vehicle designers to facilitate the efficient early stages of a detailed design process.²⁰ The objective is to maintain design freedom while simultaneously improving the probability of mission success. M-SAPE combines systems engineering modules that incorporate flight mechanics, aerodynamics, aerothermodynamics, structural analysis, impact analysis, thermal soak, and thermal protection systems.²⁰ M-SAPE is a modified version of the System Analysis for Planetary Entry Descent and Landing (SAPE) code developed as a system of a systems manager utilizing the Multi-Mission Earth Entry Vehicle (MMEEV) design code which has evolved during the last decade.²⁹ When employed for entry vehicle conceptual design studies, M-SAPE utilizes a *Python* language framework to integrate a suite of multidisciplinary platforms, including POST2, Direct Simulation Monte Carlo (DSMC), LAURA, and conventional CFD methods, along with wind tunnel and experimental flight data.²⁰ This system of systems approach can substantially reduce the time required for concept development studies to hours instead of days or even weeks, ensuring a high level of confidence. A flow chart depicting the M-SAPE overall solutions process for a typical simulation run is shown in Figure 7.²⁰

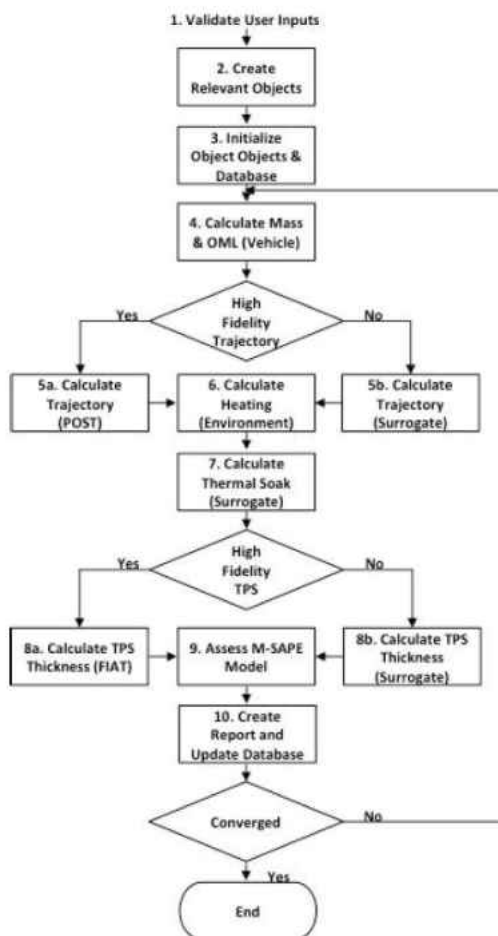


Fig. 7. M-SAPE Flow Chart²⁰

*FIAT,³⁰ stands for Fully Implicit Ablation and Thermal Analysis Program, which is was not used during the course of this study.

CHAPTER 3

METHODOLOGY AND PROCEDURE

The objective of this research has been to assemble a robust and validated aerothermodynamic database for a potential Mars sample return Earth-entry vehicle. This has been accomplished by estimating peak heating over a wide range of possible vehicle geometries, masses, return velocities, and entry trajectories. By eliminating possible vehicle design enhancements such as lifting body flight control, M-SAPE facilitates rapid concept design analysis. Achievement of this goal was attained by utilizing fundamental knowledge along with the engineering analysis tools described earlier, thus enabling the validation of the data collected.

3.1 BASELINE MODEL

Since the successful re-entry of the Earth-orbiting Vostok spacecraft in 1961, a range of Earth-return Earth-entry vehicles has been designed and flown. The actual, validated characteristics of those entry systems represent the most reliable data set on which the present approach can be evaluated. Consequently, Earth entry velocity, V_E , ballistic coefficient, β , and flight path angle, γ , along with sphere-cone geometric parameters for selected entry designs, are summarized in Table 1. The actual documented ranges for each parameter have been incorporated in a baseline M-SAPE matrix to establish the initial “calibration range” which will be expanded at both extremes of each parameter by 10%.

- Entry Velocity (V_E): 9.5 km/s to 14.5 km/s
- Ballistic coefficient (β): 10 kg/m² to 150 kg/m²
- Flight path angle (γ): -5.0° to -20.0°

These data enabled pragmatic constraints on the vehicle geometry and trajectory confidence levels. The ballistic coefficient was difficult to estimate since the overall drag coefficients are

Table 1. Sample Return Capsule (SRC)/Small Entry Probe Earth Entry Vehicle Characteristics

	Apollo 11 ¹⁴⁻¹⁷	Genesis ³¹⁻³³	Stardust ³⁴⁻ ₃₆	Hayabusa ³⁷⁻ ₄₀
Entry Velocity Ve (km/s)	11.057	11.04(designed) 10.8	12.8 12.9	12.2 11.65
Ballistic Coefficient β (kg/m²)	122 (Estimated Ballistic)	80	60	113.09
Entry Flight Path Angle γ (deg)	-6.48	-8.0	-8.21	-12.3 -12.7
Sphere Cone Half Angle θ (deg)	(Spherical Section, see Nose Radius)	59.8 60	60	45
Nose Radius Rn (m)	4.694	0.4394 0.4298	0.2286	0.2

unknown. However, in the absence of lift, flight path angles don't have a significant influence on ballistic atmospherics, which left a wide range of entry angle options open. Comparisons with actual flight data enhanced overall confidence in this study.

3.2 POST2 ANALYSIS

The parametric ranges for entry velocity, ballistic coefficient, flight path angle and geometric characteristics for a range of spherically blunted cone angles, from 45° to 60°, were used as input variables in the POST2 code. POST2 was employed to analyze the trajectory characteristics for each combination of entry velocity, ballistic coefficient, and flight path angle. The resulting data incorporated associated local atmospheric density, pressure, and temperature,⁴¹ and generated instantaneous estimated local convective heat flux and relative velocity at various altitudes proceeding along the entry trajectory. From these simulations, maximum estimated heat flux, along with the associated relative velocity and local atmospheric parameters, were compiled for further analysis.

3.3 LAURA ANALYSIS

Data collected from the POST2 analysis have been used to estimate peak heat flux levels for convective and radiative heating, employing the Langley Aerothermodynamic Upwind Relaxation Algorithm (LAURA). In order to estimate reliable convective and radiative heating levels for each case, the LAURA CFD code was employed to characterize the high hypersonic boundary- and entropy-layer flow behavior. The Hypersonic Air Radiation Algorithm (HARA)²² code was coupled with converged LAURA solutions to numerically predict the radiative heat flux. Both POST2 and the associated CFD (LAURA/HARA) runs were first evaluated using the historical baseline entry vehicle flight parameters summarized in Table 1. Subsequently entry body cone angles between 45 degrees and 60 degrees, in 5-degree increments, were simulated. The resulting data from the CFD analyses was compiled to produce the aerothermodynamic database, which has been the focus of this study.

CHAPTER 4

RESULTS

4.1 TRAJECTORY RESULTS

In order to evaluate a wide range of Earth return trajectories for each of the defined entry-vehicle geometries, POST2 was employed to evaluate the altitude at which maximum heating was predicted to occur, based on entry velocity, flight path angle, and ballistic coefficient. The Python script *Run_POST_All.py* was used to simulate all of the possible combinations of entry velocity, flight path angle, and ballistic coefficient, using POST2. Every trajectory evaluated in POST2 generated a Matlab output file which contained altitude-based atmospheric data, relative local velocity, and heat flux, corresponding to each altitude. The Python script *Process_Matlab_Files_POST2.py* extracted the data associated with the altitude at which maximum heating occurred for each run, and then exported the data into an Excel file. Table 2 shows how the associated data obtained from each POST2 run was tabulated. There were 1,936 POST2 trajectory runs for each of the four prescribed cone angles (45°, 50°, 55°, 60°), generating 7,744 simulation result sets.

Table. 2. Representation of POST2 results

Altitude (m)	Atmospheric Temperature (K)	Density (kg/m ³)	POST Convective Heat Flux (W/m ²)	POST Convective Heat Load (J/m ²)	Relative Velocity (m/s)
...
46897.38	269.40	0.001517	21124795.45	191413335.70	12270.45
...

A composite plot of the relative velocity associated with the maximum heat flux for entry velocity and ballistic coefficient on the x-axis and cone angle and flight path angle on the y-axis

for every combination is shown in Figure 8. The resulting correlation showed that cone-angle and ballistic coefficients did not have a significant impact on the relative velocity associated with maximum heating. However, flight path angle and, more obviously, entry velocity exhibited

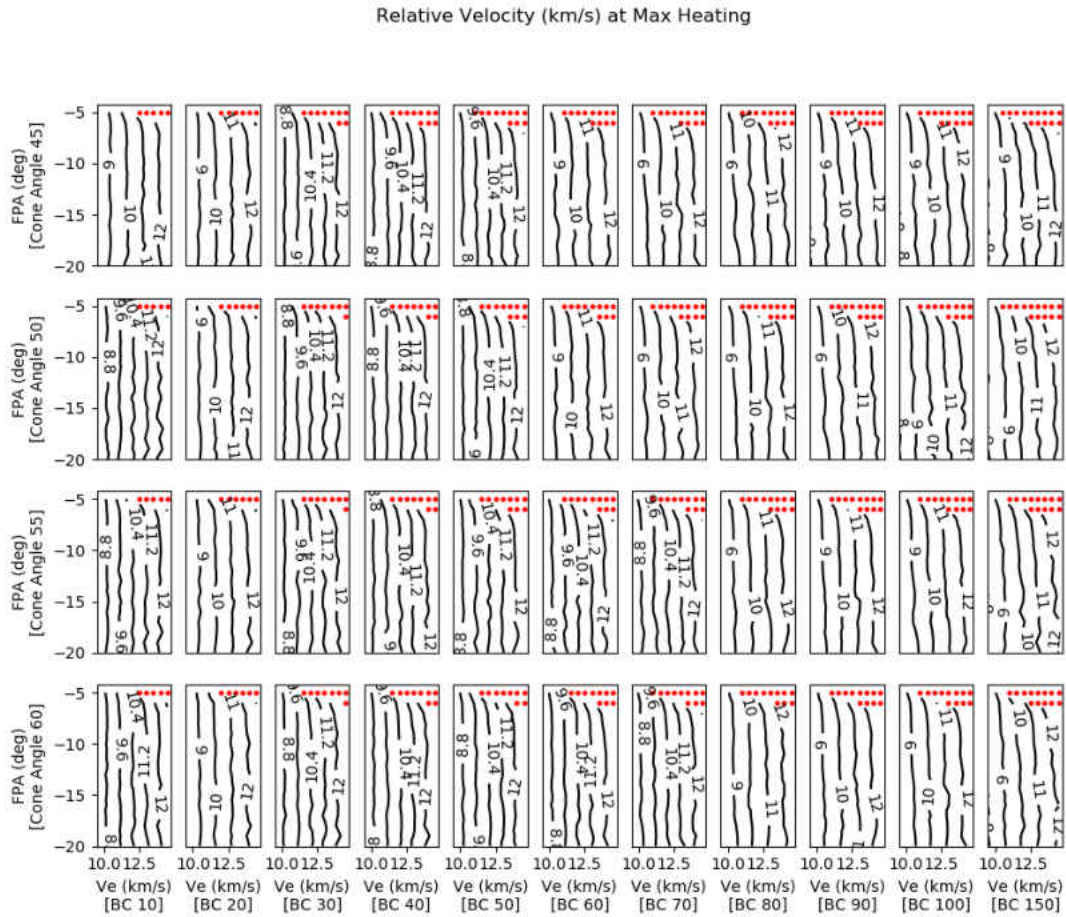


Fig. 8. POST2 results showing case-by-case relative velocity for maximum heating.

a significant influence on the relative velocity at which maximum heating occurs. In Figure 8, and in subsequent figures, the red dots indicate maximum heating data points associated with entry angles that were considered to be too shallow for further consideration, because those delineated trajectories were likely to cause the entry vehicle to skip back out of the space. Under

those circumstances, the probability that the sample return capsule would be captured within the terrestrial atmosphere was considered to be unacceptably low.

Relative velocity is important for guiding more-detailed investigations of convective and radiative heat flux, utilizing comprehensive LAURA-based CFD analyses. In the near term, examining estimated convective heat flux and integrated heat loads obtained by employing POST2 provided important insights regarding the relationship between entry vehicle geometry (ballistic coefficient and cone angle), entry velocity, and entry flight path angle. Estimates of the maximum convective heat flux, utilizing the POST2 simplifications for each of the specific cone angle- and ballistic coefficient-based geometries, when subjected to different combinations of entry velocity and flight path angle, are displayed in Figure 9. It is certainly logical to conclude that as the entry velocity increases, the resulting maximum heat flux increases. Since ballistic coefficient increases linearly with mass, higher maximum heat flux values correlate with increasing ballistic coefficient, as well. An interesting observation, however, is that cone angle did not appear to significantly affect maximum heat flux predictions. The data showed that, for shallower flight path angles, lower maximum heat flux levels resulted. However, steeper entry angles did not produce maximum heat flux magnitude increases as large as had been anticipated. A plausible explanation could be that the entry vehicle slows down more rapidly at these steeper flight path angles, resulting in lower velocities as the entry vehicle descends into the denser portion of the atmosphere where viscous heating from higher relative velocities could be more severe.

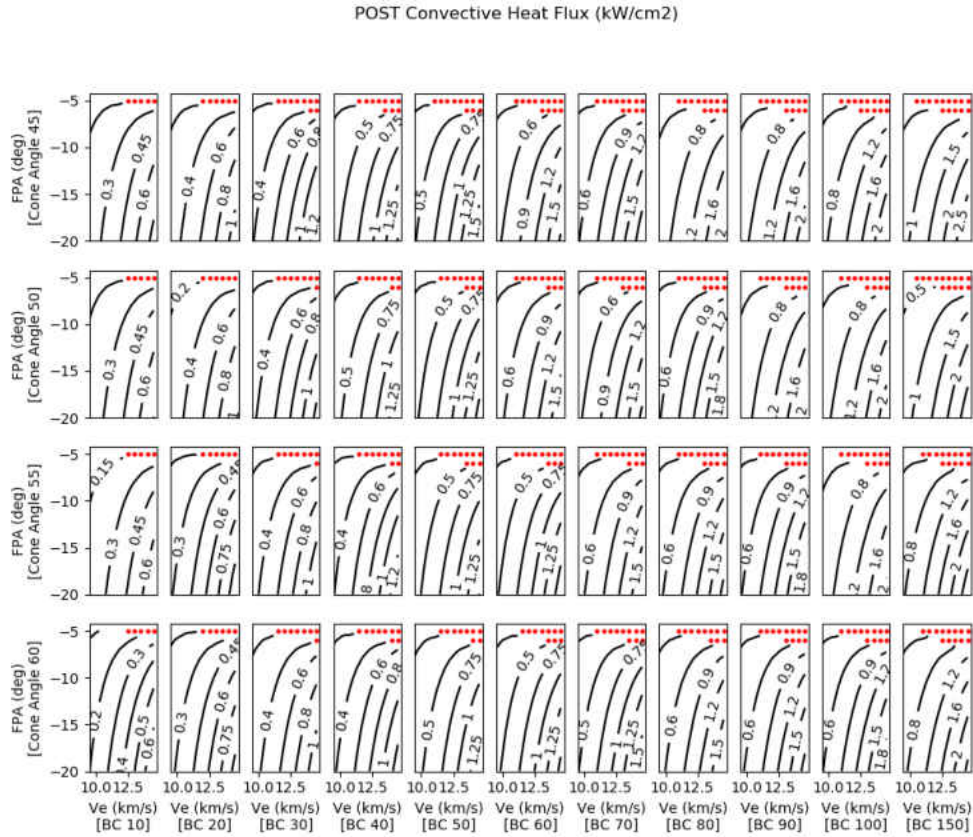


Fig. 9. Approximate maximum convective heat flux, correlated with flight path angle (FPA), and entry velocity (Ve) for various combinations of cone angle and ballistic coefficient (BC).

Figure 10 is a plot of estimated total convective heat load (kJ/cm²), employing POST2, in terms of flight path angle and entry velocity, over the range of cone angles and ballistic coefficients considered in this study. Increases in entry velocity produced increases in total heat load. However, in contrast with entry velocity, shallower entry flight-path angles corresponded with higher total convective heat loads. A shallow entry angle extends the time during which the entry vehicle resides in the less-dense outer atmosphere, thereby reducing its velocity as it enters the denser portion of the atmosphere where maximum heating occurs. This also means that the entry vehicle decelerates at a slower rate, incurring atmospheric entry heating for a longer period of time, resulting in larger overall heat loads. Cone angle changes did not appear to significantly

impact the resulting total convective heat load; however, higher ballistic coefficients resulted in higher heat loads, due to the increases in vehicle mass.

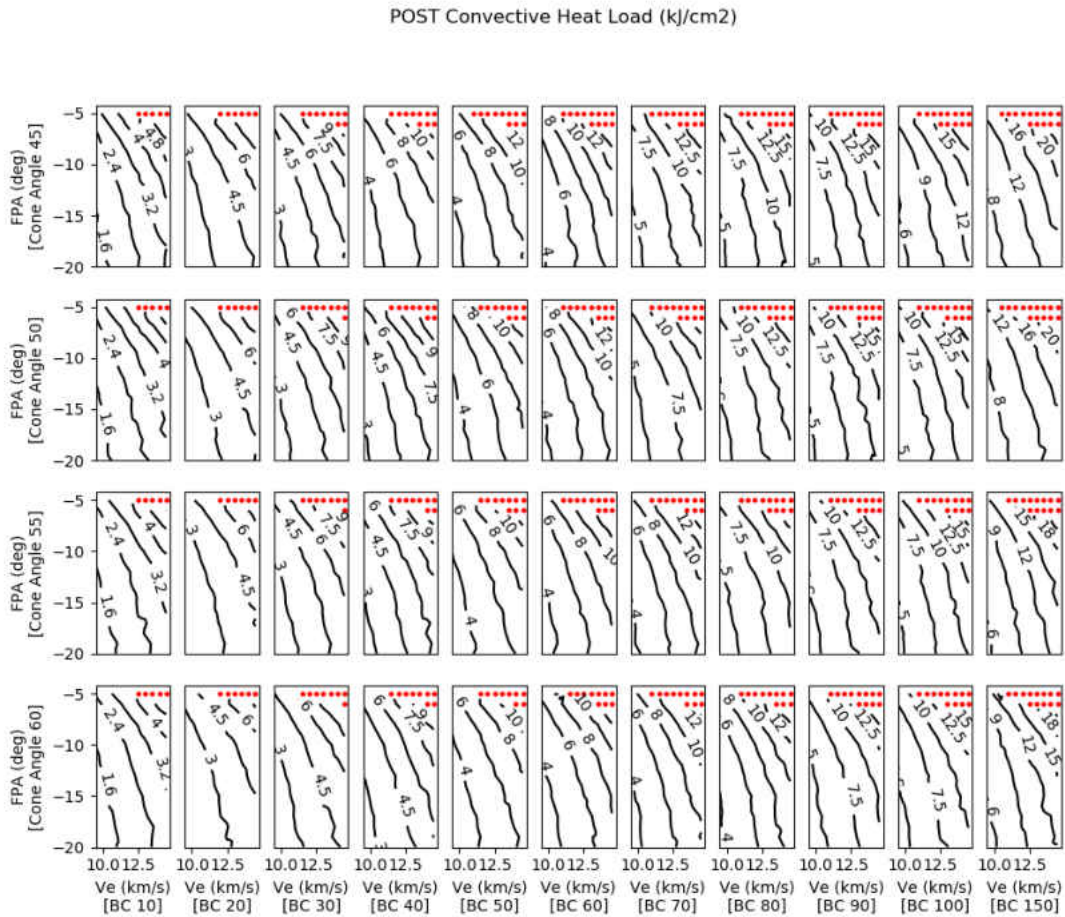


Fig. 10. Approximate maximum convective heat loads correlated with flight path angle (FPA), and entry velocity (V_e) for different cone angles and ballistic coefficients (BC).

The POST2 simulations show that high entry velocities produced higher maximum local heat fluxes and total heat loads. This is an obvious observation; however, with respect to entry vehicle configuration, convective heating magnitudes are most sensitive to ballistic coefficients

based on vehicle mass, rather than on cone angle geometries. Since convective heating is only one consideration at higher hypersonic velocities, further evaluation is needed to better approximate convective heating, along with associated radiative heating. This can be done through expanded computational fluid dynamics analyses, utilizing LAURA.

4.2 LAURA CFD RESULTS

Had this investigation attempted to estimate the maximum heat flux occurring in the 7,744 possible discrete combinations of entry vehicle geometries and entry trajectories utilizing the LAURA CFD code, the time required and associated resource costs would have been both excessive and impractical. In order to expedite the process, 50 specific cases were selected for four cone angles. This resulted in 200 LAURA CFD runs. The python script *LAURA_TEST.py* was used to run those cases iteratively, until converged solutions were obtained. LAURA input parameters included: relative velocity (at the maximum estimated convective heat flux obtained from each POST2 study); the specific atmospheric density (kg/m^3), temperature (K), and associated angle of attack (taken to be 0 degrees, since this study focused exclusively on ballistic entry trajectories).

Achieving convergence for high energy, non-equilibrium flows utilizing LAURA can be difficult, especially due to the large array of variable parameters that affect the local individual flow properties. In order to efficiently and effectively run the 200 selected cases with LAURA, careful specification of a proper grid size for the modeled geometry and flow field was necessary, along with an implementation of the appropriate numerical simulation settings, in order to facilitate grid alignment and computational time step sizes, while simultaneously satisfying Jacobian constraints and implementing transport property updates. As a consequence, baseline sets of LAURA cases were run, in order to determine appropriate values for subsequent

computations. One *case of interest* for each cone angle was selected from each of the four 50-case lists identified for more-detailed LAURA analyses. Table 3 summarizes the selected baseline cases along with the associated properties employed for each cone angle baseline.

The LAURA run specifications were adjusted by trial and error until converged solutions demonstrated that this tolerance was met. A second convergence criterion for establishing solution convergence was a thorough examination of the spatial variation of the computed local heat flux through the boundary layer. Figures 11 and 12 consist of calculated convective heat flux values on the y-axis; the x-axis represents the length of the vehicle body where the plotted line depicts heat flux values along the fore-body of the vehicle. Figure 11 shows a non-converged solution exhibited physically impossible local heat flux variations and discontinuous jumps.

Table 3. *Parameters required to initiate baseline LAURA runs, along with specified initial conditions (relative velocity, atmospheric density and temperature)*

Cone Angle (deg)	V entry (m/s)	BC (kg/m ²)	FPA (deg)	Relative Velocity (m/s)	Density (kg/m ³)	Atmospheric Temperature (K)
45	14500	150	-12	12270	0.0015174	269.40
50	11000	80	-19	9265	0.0013659	270.65
55	13500	20	-15	11661	0.0002200	239.60
60	14500	150	-18	12147	0.0019792	264.03

Conversely, fully-converged solutions exhibited relatively smooth, asymptotic profiles. The large spatial variations in Figure 11 indicated significant solution error levels, and convergence had not been achieved. Figure 12 shows a much smoother plot of spatially-varying convective heat flux,

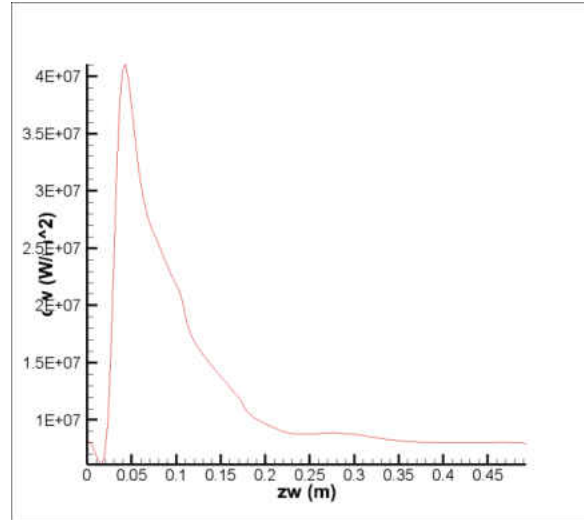


Fig. 11. Non-converged LAURA solution for convective heat flux (q_{conv}) vs. the grid x -axis

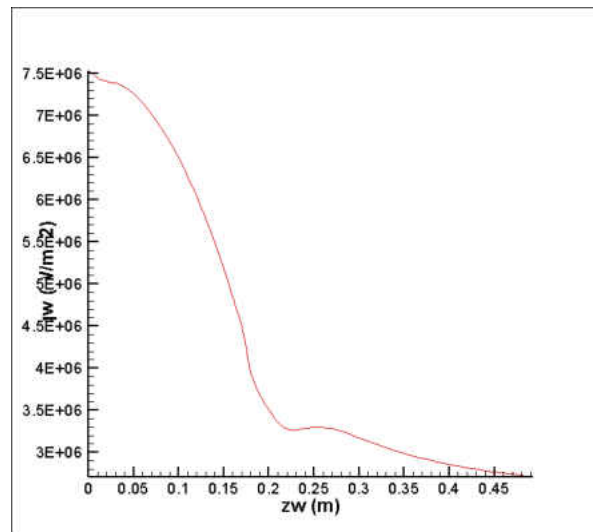


Fig. 12. Converged LAURA solution for convective heat flux, $q_{conv}(x)$ vs. the grid location on the x -axis.

with plausible variations that involve local chemistry and possible radiative coupling effects. Once the acceptably converged LAURA/HARA baseline cases were verified, the specific run parameters were applied to the remaining cases in the specific cone geometry set. The convective and radiative heat flux distributions, plotted along the sphere-cone z -coordinate axis for each LAURA/HARA case, were plotted and examined. Summary data were

compiled from the respective solution files for all of those runs; a representative entry is displayed in Table 4.

Table 4. Representation of a LAURA/HARA result

L2 norm (x10 ⁻⁸)	Cone Angle	Entry Velocity m/s	Ballistic Coef. (Kg/m ²)	Flight Path Angle	Relative Velocity m/s	Density kg/m ³	Temp °K	Max Convective Heat Flux W/m ²	Max Radiative Heat Flux W/m ²	Max Total Heat Flux W/m ²
5.12	45°	10,000	20	-8°	8,588.08	0.000146	231.02	3,428,839	53,0876.83	3,4821,926

The Residual L2 norm was used to determine whether a run had converged. L2 norm values less than or equal to 1.00E-8 were employed as the maximum allowable threshold for an acceptably-converged solution. If a LAURA/HARA solution had an L2 norm value greater than that threshold, it was removed from the data set. The converged LAURA/HARA results were then compiled into a *finalized data set*. Employing that data, the local atmospheric density

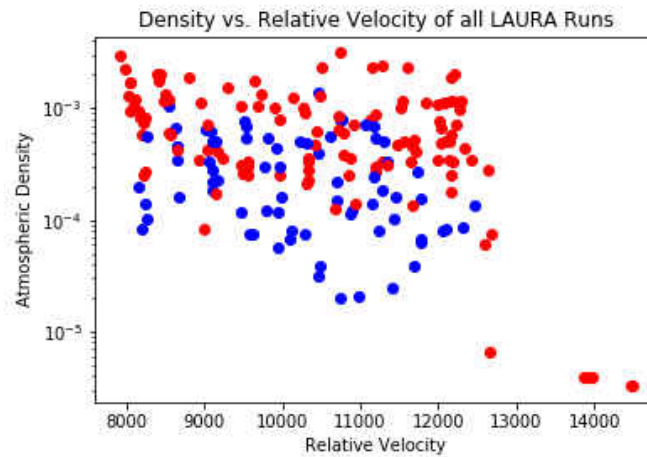


Fig. 13. Atmospheric Density and Relative Velocity at maximum total heating for all LAURA/HARA runs. Blue dots represent converged solutions, while red dots represent non-converged solutions.

($\log_{10} \rho$ (kg/m³)) and relative velocity (m/s) resulting in maximum heating for that case were subsequently plotted in order to investigate the probable causes for failed (non-converged) solutions. Figure 13 shows the distribution of L2-converged solutions (blue dots) and non-converged runs (red dots). Failed runs were mostly associated with high relative velocity-high density cases ($V \geq 12$ km/s, $\rho \geq 0.0003$ kg/m³), which were also attributable to steep flight path angles, wherein the entry vehicle penetrated a denser portion of the atmosphere very quickly, with insufficient time to decelerate to more moderate velocities. Other non-converged solutions were likely a result of non-compliant LAURA run parameters, such as mesh and shock alignment for specific cases, which were needed to establish a proper flowfield convergence. Those particular results were not used for further analysis.

The relative velocity-density altitude contours at which maximum stagnation convective and radiative heat fluxes occur have been plotted in Figures 14 through 17. Because of the substantial variation in density altitude over the various cases, a \log_{10} scale of density has been employed as the vertical axis. These figures show lower heat flux resulting from increased cone angles. It was also imperative to investigate the resulting surrounding environment, namely the atmospheric density and relative velocity of the vehicle at which maximum heating occurs. The resulting figures show that, as is intuitive, as density and velocity increased, heat flux amplified as well.

An important function of examining the velocity and density profiles was to ensure that the resulting data makes sense for further analysis. By removing data points for LAURA runs that were non-converged solutions, a more high fidelity model could be assembled from verified data. By observing the contour plots of convective and radiative heat flux correlations for relative velocity and atmospheric density at maximum heating, it can be ascertained that the data

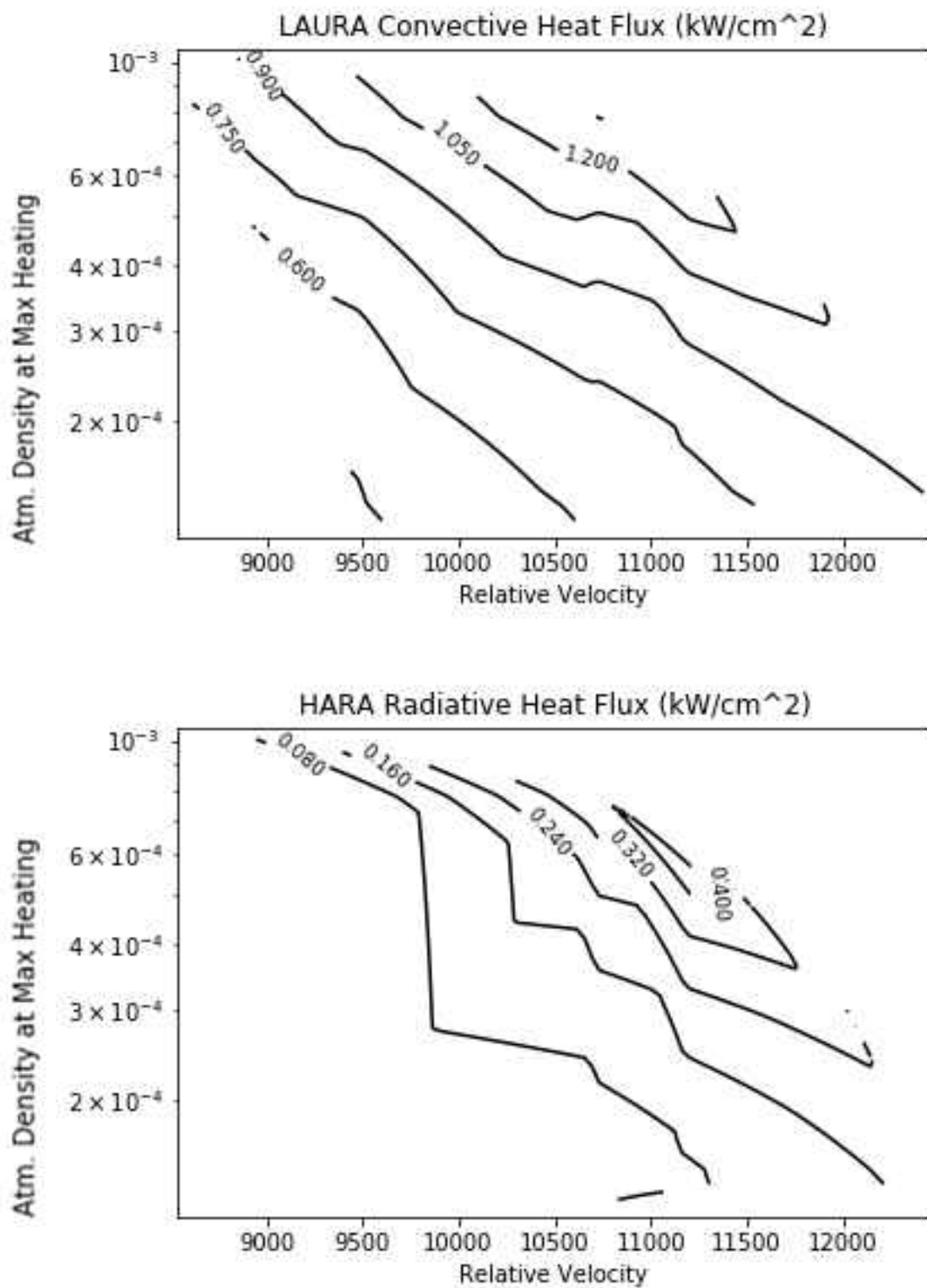


Fig. 14. LAURA/HARA Results for 45 Degree Cone Angle, correlating Atmospheric Density ($\log_{10} \rho$, kg/m³) with Relative Velocity (m/s) for Maximum Stagnation Heating.

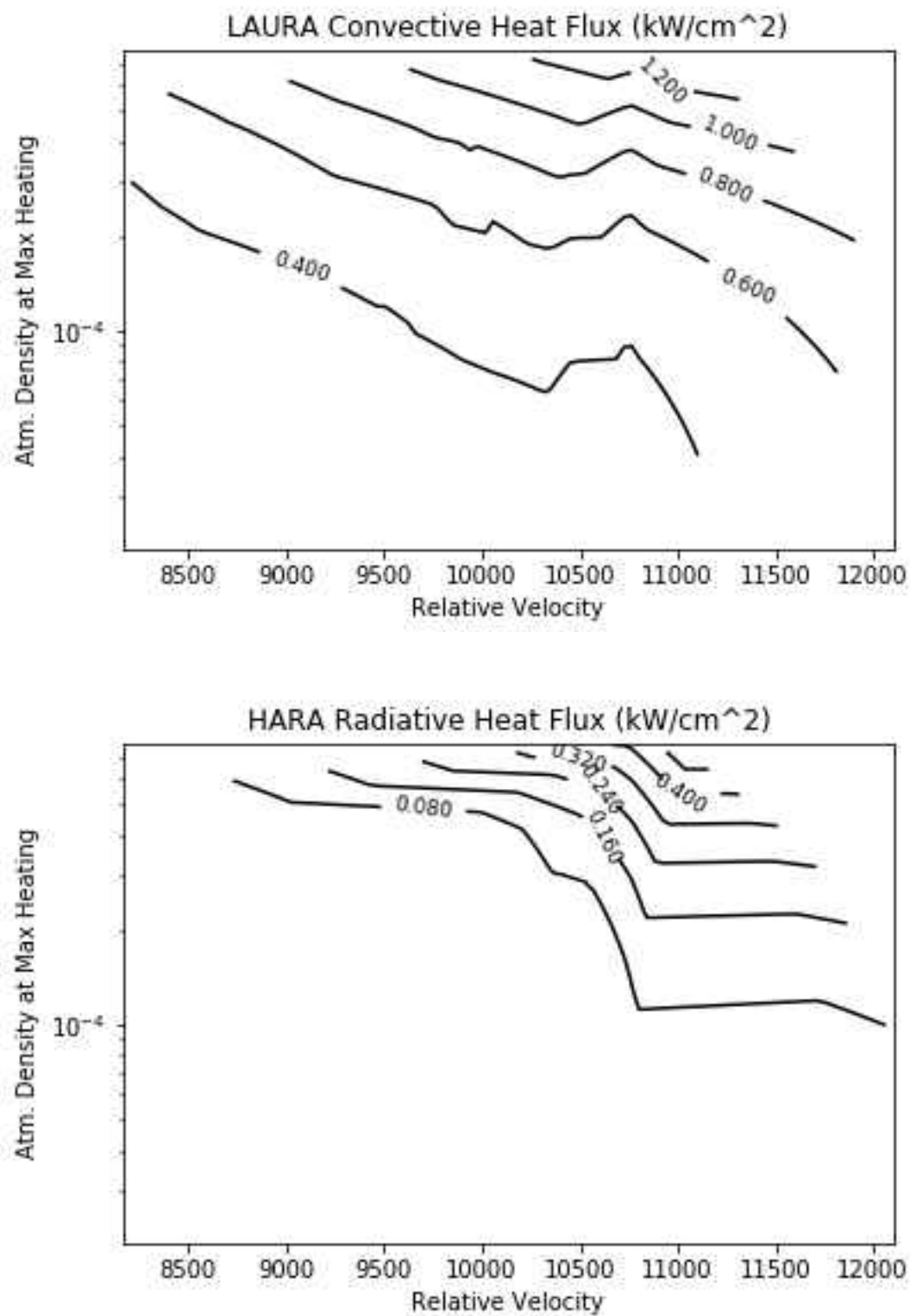


Fig. 15. LAURA/HARA Results for 50 Degree Cone Angle, correlating Atmospheric Density ($\log_{10} \rho$, kg/m³) with Relative Velocity (m/s) for Maximum Stagnation Heating.

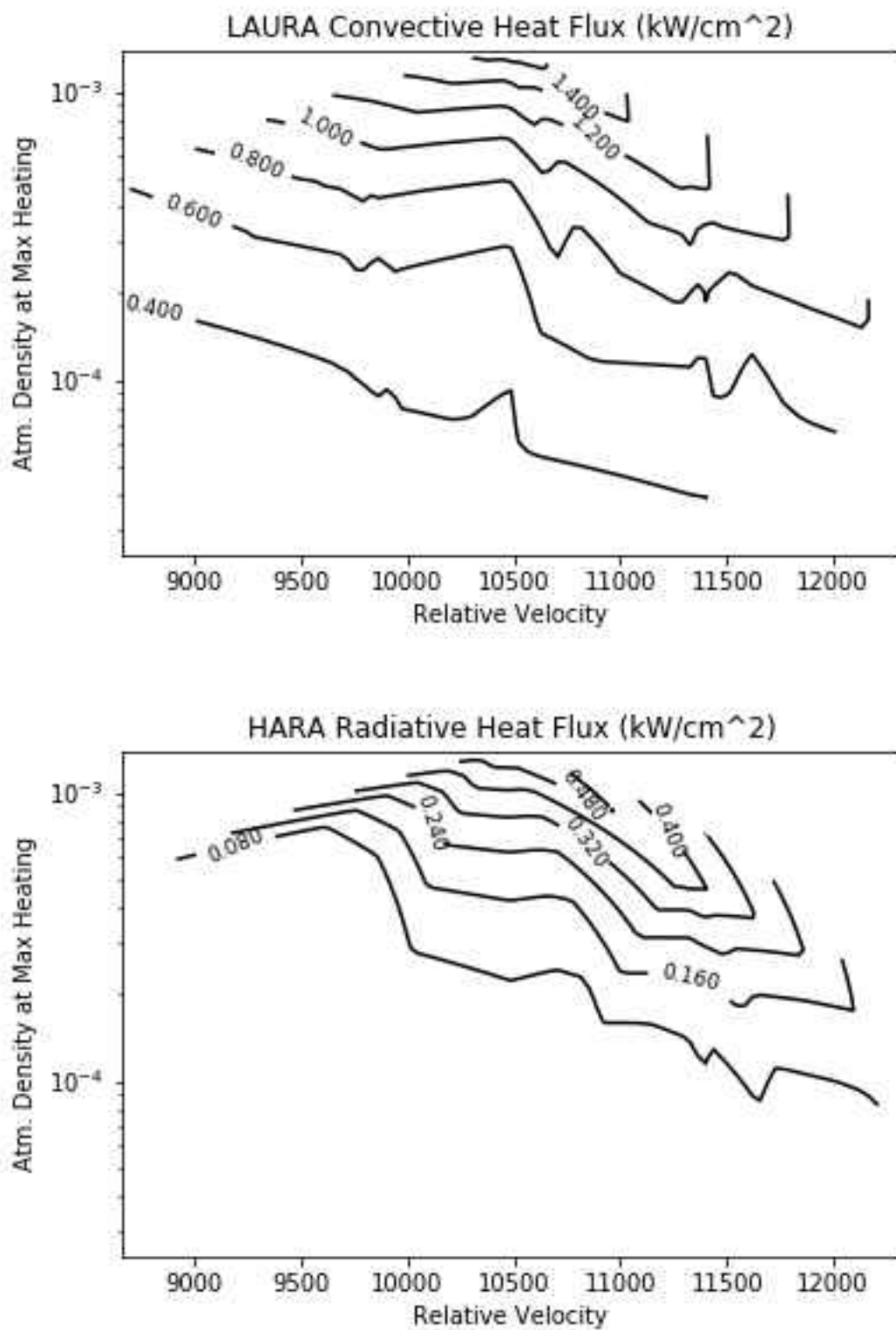


Fig. 16. LAURA/HARA Results for 55 Degree Cone Angle, correlating Atmospheric Density ($\log_{10}\rho$, kg/m³) with Relative Velocity (m/s) for Maximum Stagnation Heating.

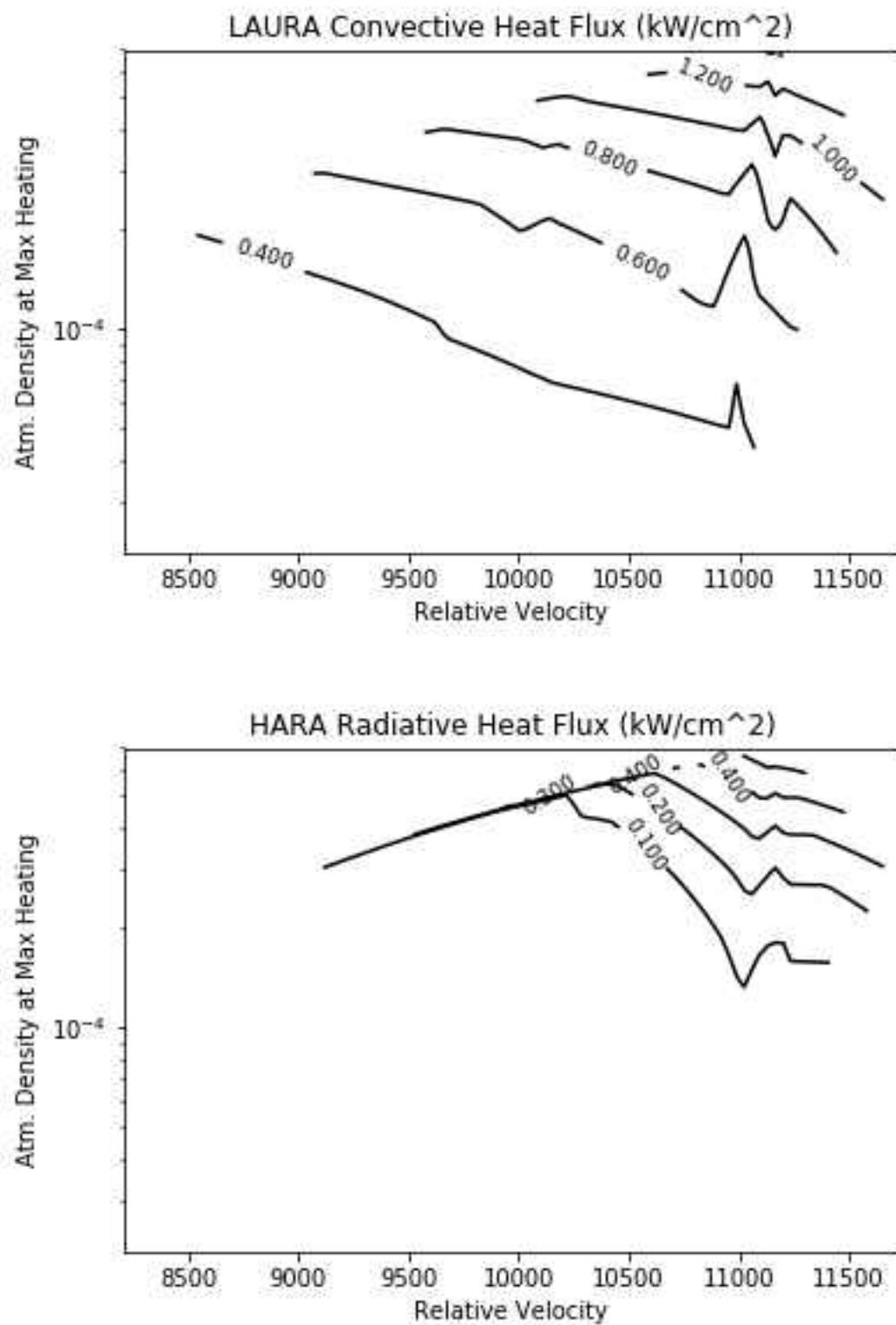


Fig. 17. LAURA/HARA Results for 60 Degree Cone Angle, correlating Atmospheric Density ($\log_{10}\rho$, kg/m^3) with Relative Velocity (m/s) for Maximum Stagnation Heating.

compiled from the successful LAURA runs are good estimations for an aerothermodynamic database, since contour lines follow a relatively even path with minor variability. A larger group of LAURA runs would be optimal in increasing the fidelity of the model; however, since these CFD runs require a large amount of time to conduct, this option is not viable at this time. Therefore, a variance-based analysis was conducted to establish a statistical model of LAURA data, in order to expand on, as well as to establish, estimated error within the existing model.

4.3 SURROGATE MODEL DEVELOPMENT

A variance-based adaptive model was used to build an approximate surrogate model, based on the data attained from LAURA calculations (actual model), by employing a polynomial decomposition approach where the new model coefficients were computed by regression. The model is represented as:

$$\dot{q} = A V_e^B \theta^C \beta^D \Upsilon^E \quad (12)$$

where A, B, C, D and E are the coefficients needed to build the surrogate model and the remaining variables are input values obtained from previous analysis, and where q denotes heat flux calculated with LAURA (either convective or radiative), V_e denotes the entry velocity, θ represents cone angle, β represents ballistic coefficient, and Υ represents flight path angle. The \log_{10} of equation (12) was taken:

$$\log_{10}(\dot{q}) = \log_{10}(A) + B \log_{10}V_e + C \log_{10}\theta + D \log_{10}\beta + E \log_{10}\Upsilon \quad (13)$$

And equation (13) was then used to calculate the coefficients A, B, C, D and E in the form of:

$$[M][x] = [F] \quad (14)$$

Where $[M]$ is a 5x115 matrix, every row consisting of the form:

$$1 + \log_{10}Ve + \log_{10}\theta + \log_{10}\beta + \log_{10}Y \quad (15)$$

For each converged LAURA solution input parameter set. The column $[x]$ represents the unknown vector:

$$\begin{bmatrix} \log_{10}A \\ B \\ C \\ D \\ E \end{bmatrix} \quad (16)$$

And $[F]$ representing a 1x115 matrix, where each row is a $\log_{10}(\dot{q})$ for each corresponding LAURA heat flux solution to matrix $[M]$. Equation (14) was then formulated as:

$$[M][M]^T [x] = [F][M]^T \quad (17)$$

Equation 17 was then solved for x, to find the corresponding coefficients for the expanded approximate surrogate model. Figures 18 and 19 show a comparison actual and approximate convective and radiative heat fluxes, respectively. Figure 19 shows a relatively good fit line

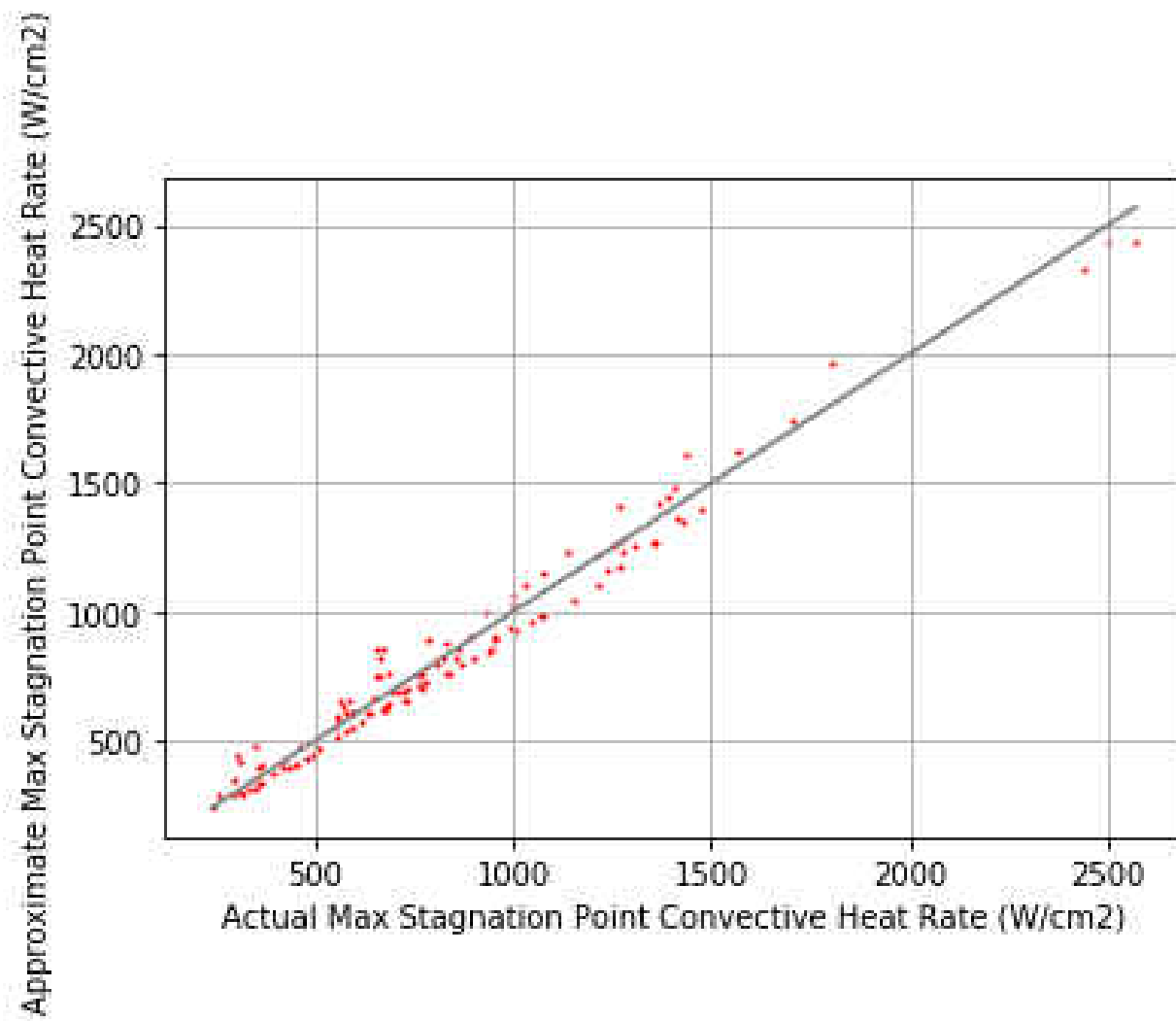


Fig. 18. Comparison of Actual Convective Heat Flux (LAURA results) vs. Approximate Convective Heat Flux (Surrogate Model).

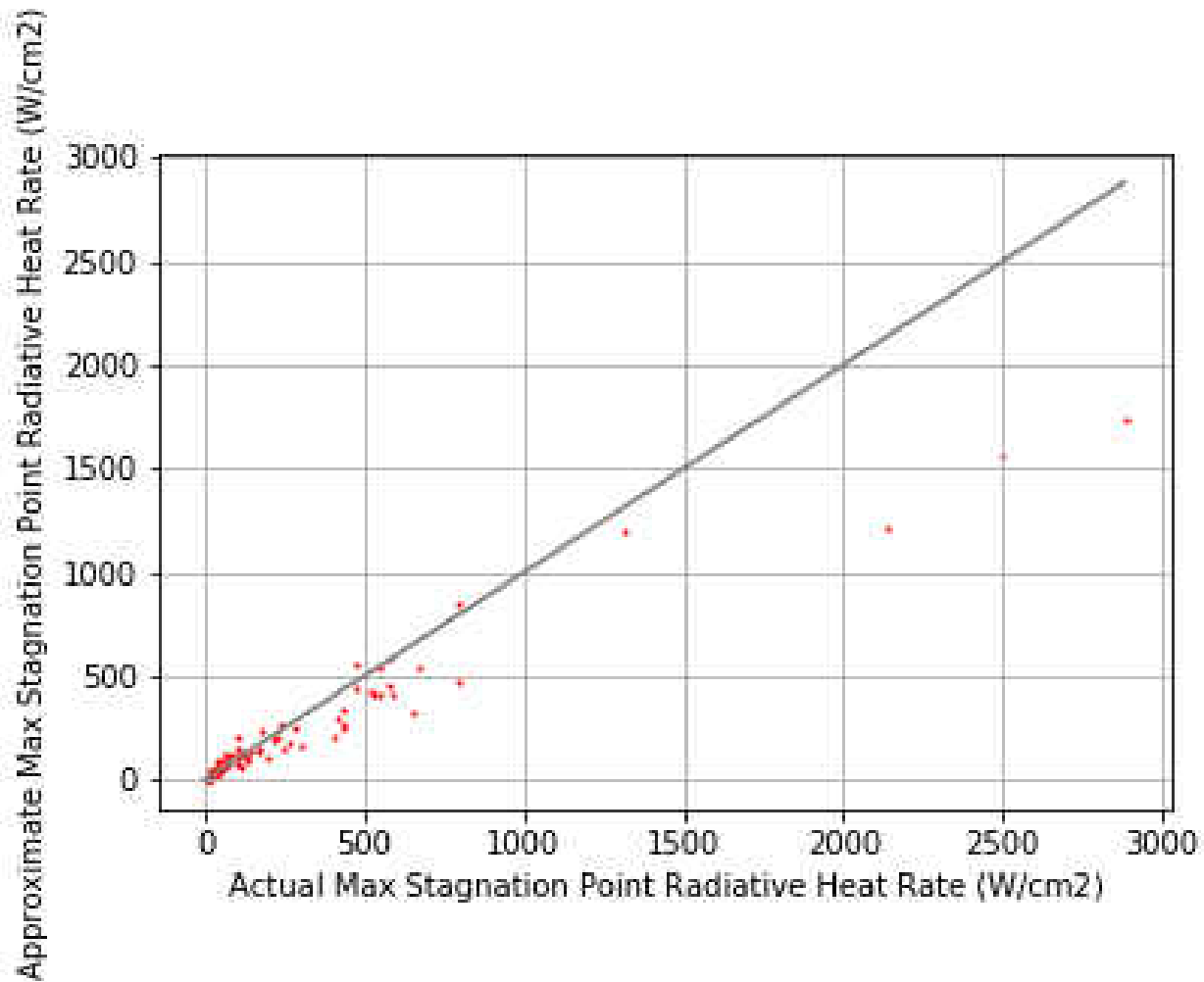


Fig. 19. Comparison of Actual Radiative Heat Flux (LAURA results) vs. Approximate Radiative Heat Flux (Surrogate Model).

for the convective model, indicating a high level of accuracy. Figure 19 also shows a relatively good fit between the approximate and the actual models, primarily for the lower level radiative heat flux values up to about 1500 W/cm². Beyond that, the model shows fairly high levels of discrepancy; however, radiative heating levels of more than 2000 W/cm² are not common and can be associated with unrealistic trajectories that would not be used for a Mars sample return. Table 5 shows the error in both the convective and radiative surrogate models. The convective surrogate model showed very low percent error and indicated a high reliability approximation

Table 5. *Error of Surrogate Models for Convective and Radiative Heat Flux.*

Error Type	Convective	Radiative
Mean Fit Percent Error	7.88542	34.1132
STD Fit Percent Error	7.33434	29.2533

to the expanded LAURA convective heat flux values. The radiative surrogate model indicates a higher percent error, due to the large discrepancies found in high-level radiative heat flux values (above 1500 W/cm²). However, most radiative heat flux values, in W/cm², range from the low hundreds to around nine hundred; the higher percent error shown in Table 5 did not significantly affect total heating when combined with convective heat flux values ranging into the thousands.

In order to accurately show the correlations between the trajectory and the geometry parameters for the various cases for a Mars sample return vehicle, a composite plot relating cone angle (CA) and ballistic coefficient (BC), with flight path angle (FPA) and entry velocity (V), and with corresponding convective and radiative heat flux contours are shown in Figures 20 and 21, respectively. These relationships show, for both convective and radiative heating, an increase in entry velocity. The more steep flight path angle results in higher heat flux levels, which is an intuitive observation, since the vehicle will be traveling at greater velocities through more dense portions of the atmosphere. Radiative heating begins to be a contributor to total heat flux at entry velocities of 11km/s, and only when associated with steeper flight path angles and ballistic coefficients of 50 kg/m² or greater. An increase in ballistic coefficient corresponds to higher levels of heat flux for both convective and radiative heating; however, at low entry velocities,

ballistic coefficient becomes a much less important factor, although, for convective heating, a higher ballistic coefficient does begin to impact heat flux values at around 60 kg/m².

Surprisingly, cone angle does not affect heat flux values at a significant level. For convective heating, a larger cone angle will result in lower heat flux, although it is a shallow variation between 45 degree and 60 degree cone angles. Cone angles affect radiative heating at even less of a noteworthy magnitude than convective heating, although an important

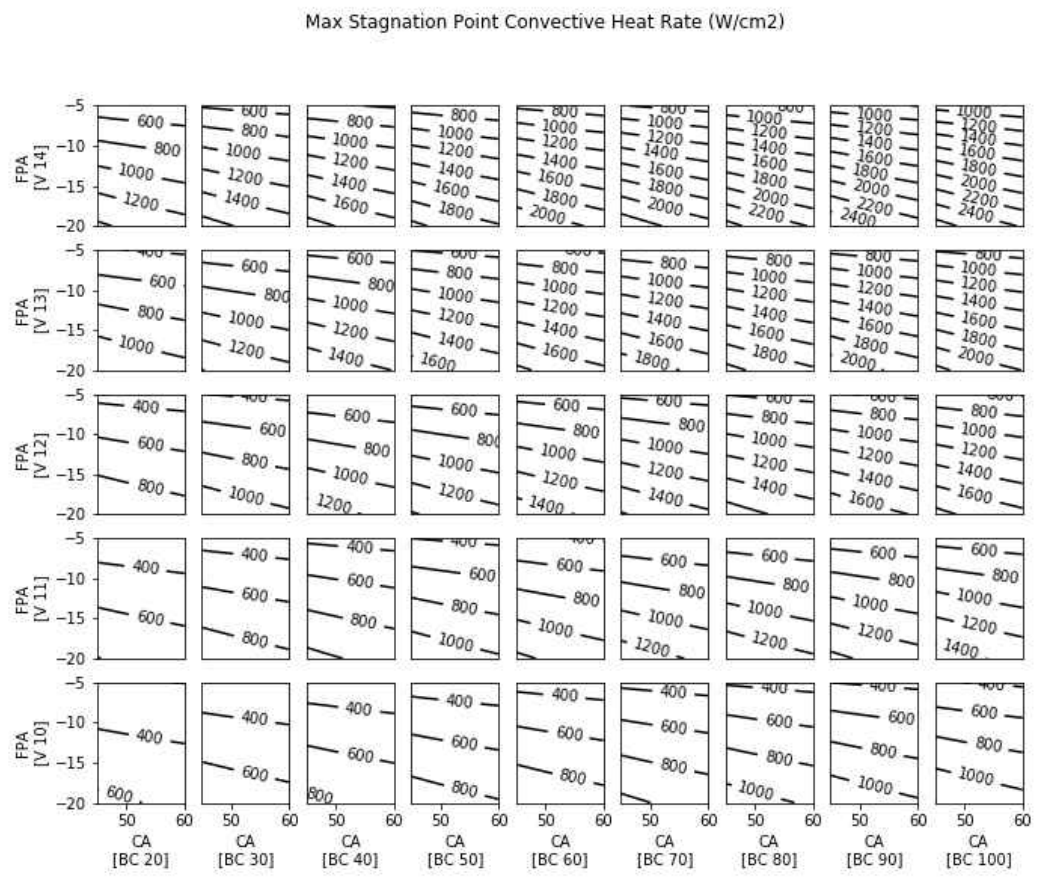


Fig. 20. Maximum Stagnation Point Convective Heat Flux Surrogate model based on LAURA results.

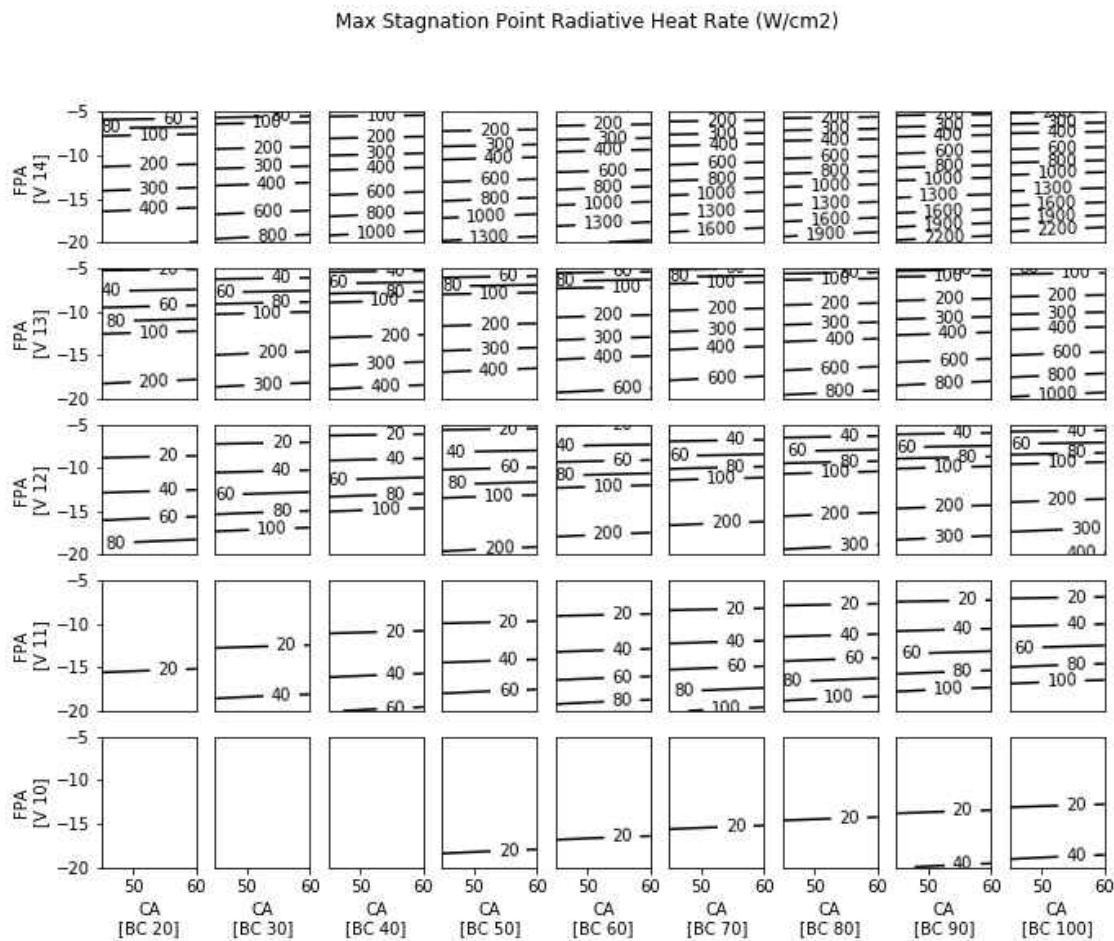


Fig. 21. Maximum Stagnation Point Radiative Heat Flux Surrogate model based on
LAURA results

observation is that as cone angles become larger, radiative heat flux values gradually increase, which is the opposite of what was seen with the relationship of cone angle and convective heating. Overall, flight path angle turned out to be the largest contributing factor to overall maximum heating values, in addition to initial entry velocity.

CHAPTER 5

CONCLUSIONS AND FUTURE WORK

It is critically important to have reliable aerothermodynamic heating estimates when proceeding with the thermal protection system design for the Mars Sample Return (MSR) Earth Entry Vehicle. In addition to geometrical trade-offs, the entry flight path angle is a major consideration because the combination of entry vehicle geometry and flight path angle are key elements that control payload survivability and recovery. This study has shown that the MSR cone-angle does not have a major impact on overall heating, although lower maximum levels of stagnation convective heating occur as the cone angle is increased. Conversely, radiative heating increases as cone angle increases, but variances between cone angles are not highly significant. The entry flight path angle and ballistic coefficient (as influenced by overall entry vehicle mass) have greater impacts on aerothermodynamic heating, especially at the higher entry velocities that will surely occur for a Mars-Earth return mission.

Cone angle results do not produce a major influence on maximum overall heat flux, but a 45° cone produces slightly higher maximum heat flux than the larger cone angle geometries. The higher heat flux can possibly be offset by reducing overall entry vehicle mass via reduced heat shield mass based on thermal protection system material selection. Other possibilities that can be justified from this study include the possibility of optimizing the cone angle geometry based on such considerations as center-of-mass flight control and return sample storage and protection. Conversely, a 45° cone would be better able to experience more stable flight and a lower g-force impact with the ground.

At the high anticipated Mars-return entry velocities, this study appears to show that there are combinations of cone geometry, along with specific atmospheric entry trajectories, that can

mitigate risk by enhancing survivability without producing extreme heat flux. A more detailed study within these apparent optimal combinations can be justified. Since shallow entry angles reduce peak stagnation heating, but extend the time during which high heat flux occur, combined studies incorporating realistic thermal protection system designs should be undertaken, in order to properly assess the overall sample recover strategy, since thermal soak can be a contributing factor to sample survivability. The fidelity of the POST2 trajectory simulations compiled in this study should be adequate to enable further investigations concerning impact survivability based on vehicle geometry.

REFERENCES

- [1] Hansen, J.R., "Chapter 12: Hypersonics and the Transition to Space." *Engineer in Charge: A History of the Langley Aeronautical Laboratory, 1917–1958*. The NASA History Series. Sp-4305. United States Government Printing, 1987.
- [2] Allen, H.J. and Eggers, A.J. Jr., "A Study of the Motion and Heating of Missiles Entering the Earth's Atmosphere at High Supersonic Speeds," NACA TN 4047, 1951.
- [3] Cox, R.N., Crabtree, L.F., "Elements of Hypersonic Aerodynamics," Academic Press, 1965.
- [4] <https://www.flickr.com/photos/nasacommons/16374997425/in/photolist-fkPRoX-qX19eP-fm8HHJ-qCdEpw-fkPKtk>, (July 2018)
- [5] Prabhu, D.K., Saunders, D. A., "On Heatshield Shapes for Mars Entry Capsules," ERC, Inc., NASA Ames Research Center, Moffett Field, CA, 94035, 2012, AIAA-0399.
- [6] Hemateja, A., Ravi Teja B., Dileep Kumar, A., Rakesh, S.G., "Influence of Nose Radius of Blunt Cones on Drag in Supersonic and Hypersonic Flows," Department of Mechanical Engineering, Amrita School of Engineering, Bengaluru, Amrita Vishwa Vidyapeetham, Amrita University, India, 2017.
- [7] Traugott, S.C., "Some Features of Supersonic and Hypersonic Flow About Blunted Cones," *Journal of the Aerospace Sciences*, Vol. 29, No. 4 (1962), pp. 389-399.
- [8] Bird, G.A., "Molecular Gas Dynamics and the Direct Simulation of Gas Flows," GAB Consulting Pty Ltd; Emeritus Professor, The University of Sydney.
- [9] Vincenti, W.G., Kruger, C.H., Jr. "Introduction to Physical Gas Dynamics," Department of Aeronautics and Astronautics, Stanford University; Department of Mechanical Engineering, Stanford University.

- [10] Fay, J., Riddell, F., "Theory of Stagnation Point Heat Transfer in Dissociated Air," *Journal of Aeronautical Sciences* 25 (2), Feb 1958.
- [11] Gnoffo, P.A., Gupta, R.N., Shinn, J.L., "Conservation Equations and Physical Models for Hypersonic Air Flows in Thermal and Chemical Nonequilibrium," NASA Technical Paper 2867, Feb 1989.
- [12] Reddy, K., Fujiwara, T., "Thermally and Chemically Nonequilibrium Flow Analyzed by Park's Two-Temperature Model," 28th Aerospace Sciences Meeting.
- [13] Park, C., "Assessment of two-temperature kinetic model for ionizing air," *Journal of Thermophysics and Heat Transfer*, Vol. 3, No. 3 (1989), pp. 233-244.
- [14] Orloff, R.W., "Apollo by the Numbers: A Statistical Reference for the Manned Phase of Project Apollo," NASA SP-2000-4029, revised Sept. 2004.
- [15] Robinson, J.S., Wurster, K.E., Mills, J.C., "Entry Trajectory and Aeroheating Environment Definition for Capsule-Shaped Vehicles," *Journal of Spacecraft and Rockets*, Vol. 46, No. 1 (2009), pp. 74-86.
- [16] Walpot, Louis M.G., "Base flow investigation of the Apollo AS-202 Command Module," *Progress in aerospace sciences*, 2012, Vol.48-49, p.57.
- [17] Prabhu, D.K., Saunders, D.A., "On Heatshield Shapes for Mars Entry Capsules," ERC, Inc., NASA Ames Research Center, Moffett Field, CA, 94035.
- [18] Wood, W.A., "Radiation Coupling with the FUN3D Unstructured-Grid CFD Code," 43rd AIAA Thermophysics Conference, New Orleans, LA, 26-28 June, 2012, AIAA-2741.

- [19] Bauer, G.L., Cornick, D.E., Stevenson, R., "Capabilities and Applications of the Program to Optimize Simulated Trajectories (POST)," NASA CR-2770, February 1977.
- [20] Samareh, J. A., Glaab, L., Winski, R. G., Maddock, R. W., Emmett, A. L., Munk, M. M., Agrawal, P., Sepka, S., Aliaga, J., Zarchi, K., Mangini, M., Perino, S., Bayandor, J., and Liles, C., "Multi-Mission System Analysis for Planetary Entry (M-SAPE) Version 1," August 2014, NASA/TM-2014-218507
- [21] Sutton, K., Graves, R.A., "A General Stagnation Point Convective Heating Equation for Arbitrary Gas Mixture," NASA TR-376, 1971
- [22] Papadopoulos, P., Subrahmanyam, P., "Trajectory Coupled Aerothermodynamics Modeling for Atmospheric Entry Probes at Hypersonic Velocities," 44th AIAA Aerospace Sciences Meeting and Exhibit, Aerospace Sciences Meetings, 2006, AIAA-1034.
- [23] Johnson, J.E., Starkey, R.P., Lewis, M.J., "Aerothermodynamic Optimization of Reentry Heat Shield Shapes for a Crew Exploration Vehicle," University of Maryland, College Park, Maryland 20742, 2007.
- [24] Tauber, M.E., Sutton, K., "Stagnation Point Radiative Heating Relations for Earth and Mars Entries," Journal of Spacecraft and Rockets, Vol 28, No 1, 1991, pp.40-42
- [25] Mazaheri, A., Gnoffo, P. A., Johnston, C. O., and Kleb, B., "LAURA Users Manual: 5.4-54166," Tech. rep., NASA/TM- 2011-217092, May 2009.
- [26] Gnoffo, P.A., "Upwind-Biased, Point-Implicit Relaxation Strategies for Viscous, Hypersonic Flows," in AIAA Computational Fluid Dynamics Conference, Buffalo, 1989.
- [27] Gnoffo, P.A., "An Upwind-Biased, Point-Implicit Relaxation Algorithm for Viscous, Compressible Perfect Gas Flows," NASA Technical Paper - 2953, Hampton, 1990.

- [28] Stalker, R.J., "Post-Shock Non-Equilibrium Flows in Hypervelocity Aerodynamics," The University of Queensland, Brisbane, Australia, 1988, AIAA-459.
- [29] Maddock, R.W., "Multi-Mission Earth Entry Vehicle Design Trade Space and Concept Status (Version 2.0)," 8th International Planetary Probe Workshop, Portsmouth, VA, USA, 2011.
- [30] Chen, Y.K., Milos, F.S., "Fully Implicit Ablation and Thermal Analysis Program (FIAT)," Journal of Spacecraft and Rockets, Vol. 36, No. 3, pp 475-483, May-June 1999.
- [31] McNei, C.F., Merski, N. Jr., Riley, C., Mitcheltree, R., "Aerothermodynamic Environment Definition for the Genesis Sample Return Capsule," 35th AIAA Thermophysics Conference, Fluid Dynamics and Co-located Conferences, 2001, AIAA-2889.
- [32] Desai P.N., Qualls G.D., Schoenenberger, M.D., "Reconstruction of the Genesis Entry," Journal of Spacecraft and Rockets, Vol. 45, No. 1 (2008), pp. 33-38.
- [33] Tang, C., Wright, M., "Analysis of the Forebody Aeroheating Environment during Genesis Sample Return Capsule Reentry," 45th AIAA Aerospace Sciences Meeting and Exhibit, Aerospace Sciences Meetings, 2007, AIAA-1207.
- [34] Kontinos, D.A., Wright, M.J., "Introduction: Atmospheric Entry of the Stardust Sample Return Capsule," Journal of Spacecraft and Rockets, Vol. 47, No. 5 (2010), pp. 705-707.
- [35] Trumble, K.A., Cozmuta, J., Sepka, S., Jenniskens, P., Winter, M., "Postflight Aerothermal Analysis of the Stardust Sample Return Capsule," Journal of Spacecraft and Rockets, Vol. 47, No. 5 (2010), pp. 765-774.
- [36] Desai, P.N., Lyons, D.T., Tooley, J., Kangas, J., "Entry, Descent, and Landing Operations Analysis for the Stardust Re-Entry Capsule," NASA Langley Research Center, Hampton, VA, 23681-2199; Jet Propulsion Laboratory, Pasadena, CA 91109-8099.

- [37] Brucato, J.R., Rotundi, A., Epifani, E.M., "Sample Return Missions from Minor Bodies: Achievements, Future Plan and Observational Support," *Earth, Moon and Planets*, vol. 105, no. 2-4, 2009.
- [38] Buttsworth, D.R., D'Souza, M., Potter, D., Eichmann, T.N., Mudford, N., McGilvray, M., McIntyre, T.J., Jacobs, P.A., Morgan, R.G., "Expansion Tunnel Radiation Experiments to Support Hayabusa Re-entry Observations," University of Southern Queensland, Toowoomba, Queensland, 4350, Australia; The University of Queensland, Brisbane, Queensland, 4072, Australia; University of New South Wales, Australian Defense Force Academy, Canberra, ACT 2600, Australia.
- [39] Grinstead, J., Jenniskens, P., Cassell, A., Albers, J., Winter, M., "Airborne Observation of the Hayabusa Sample Return Capsule Re-entry," 42nd AIAA Thermophysics Conference, Fluid Dynamics and Co-located Conferences, 2011, AIAA-3329.
- [40] Takahashi, Y., Yamada, K., "Aerodynamic-Heating Analysis of Sample-Return Capsule in Future Trojan-Asteroid Exploration," *Journal of Thermophysics and Heat Transfer*, Vol. 32, No. 3 (2018), pp. 547-559.
- [41] U.S. Standard Atmosphere, 1976, U.S. Government Printing Office, Washington, D.C., 1976
- [42] Lai, S.T., "Fundamentals of Spacecraft Charging: Spacecraft Interactions with Space Plasmas," Princeton University Press. pp. 240 (2011).

Appendix A – Table of LAURA Results

Cone Angle (deg)	Entry Vel. (km/s)	BC (kg/m ²)	FPA (deg)	Rel. Vel. (km/s)	Atm. Density (kg/m ²)	Atm. Temp. (K)	Max Conv. Heat Flux (W/cm ²)	Max Rad. Heat Flux (W/cm ²)	Max Total Heat Flux (W/cm ²)
45	10	100	-19	8.4	0.002006	263.8	1076.1	18.9	1095.0
45	10	70	-16	8.5	0.001062	270.7	827.8	12.1	840.0
45	10	80	-10	8.6	0.000665	264.5	686.3	10.0	696.2
45	10.5	50	-10	9.0	0.000429	254.3	643.2	9.7	652.9
45	10.5	50	-12	9.1	0.000512	258.4	710.8	11.1	721.9
45	10.5	60	-12	9.0	0.000638	263.5	764.6	12.0	776.6
45	10.5	90	-9	9.1	0.000618	262.7	771.1	12.5	783.3
45	11	10	-12	9.5	0.000119	226.8	418.6	6.4	424.9
45	11	80	-12	9.5	0.000778	268.2	993.3	33.7	1026.9
45	11	90	-17	9.3	0.001517	269.4	1274.4	41.0	1315.5
45	12.5	10	-15	10.7	0.000153	231.9	650.5	42.4	693.0
45	12.5	30	-19	10.6	0.000567	260.7	1138.5	218.8	1357.4
45	12.5	80	-12	10.7	0.000784	268.4	1357.5	401.4	1758.9
45	13	10	-14	11.2	0.000139	230.0	691.3	62.2	751.6
45	13	150	-18	10.7	0.00314	255.0	2569.2	2138.9	4708.2
45	13	50	-13	11.2	0.000547	259.9	1275.1	439.1	1714.2
45	13	60	-17	11.2	0.00087	270.7	1567.9	797.3	2365.2
45	13	80	-12	11.1	0.00079	268.6	1476.4	650.9	2127.3
45	13.5	30	-8	11.8	0.000156	232.4	827.8	131.5	957.4
45	13.5	70	-6	12.6	6.15E-05	214.1	658.0	62.8	719.6
45	14.5	10	-14	12.5	0.000136	229.6	893.6	182.1	1072.3
45	14.5	20	-7	12.7	7.51E-05	217.7	729.0	123.3	850.0
45	9.5	50	-13	8.2	0.000588	261.6	555.3	7.9	563.2
50	10	40	-14	8.7	0.000449	255.3	578.7	8.4	587.1
50	10	60	-8	8.6	0.00034	249.1	508.0	7.5	515.5
50	10.5	150	-6	9.2	0.000356	250.1	631.8	10.0	641.8
50	10.5	30	-12	9.1	0.000284	245.1	547.0	8.1	555.2
50	10.5	30	-18	9.2	0.000413	253.4	664.8	10.4	675.2
50	10.5	40	-8	9.1	0.000223	239.9	491.7	7.2	498.9
50	10.5	50	-9	9.1	0.000331	248.5	576.3	8.5	584.8
50	10.5	80	-5	9.6	7.57E-05	217.8	360.9	5.3	366.1
50	11.5	30	-5	10.7	2.03E-05	199.8	294.8	11.4	298.7
50	11.5	30	-6	10.1	7.90E-05	218.7	420.9	8.5	429.2
50	11.5	40	-14	9.9	0.000441	255.0	861.5	46.8	908.3
50	11.5	60	-8	10.0	0.000297	246.1	734.3	32.1	766.4
50	12	10	-6	10.5	3.14E-05	205.3	316.9	4.8	321.7
50	12	10	-9	10.3	7.46E-05	217.6	429.7	9.9	439.4

50	12	100	-10	10.4	0.000633	263.3	1151.8	195.8	1347.6
50	12	90	-8	10.5	0.000396	252.5	939.2	109.9	1049.1
50	12.5	30	-16	10.8	0.000387	252.0	997.2	167.0	1164.2
50	12.5	60	-17	10.8	0.000783	268.4	1370.6	417.1	1787.7
50	12.5	60	-18	10.7	0.000855	270.5	1409.0	434.2	1843.2
50	12.5	90	-10	10.8	0.000596	261.9	1212.9	298.8	1511.7
50	13	100	-6	12.1	8.20E-05	219.4	674.0	67.6	740.3
50	13	50	-10	11.3	0.000335	248.8	1044.1	245.2	1289.3
50	13	50	-17	11.1	0.000705	265.8	1390.8	524.8	1915.5
50	13	50	-6	11.8	6.80E-05	215.7	584.0	41.0	621.5
50	13.5	150	-16	11.2	0.002341	260.7	2441.4	2501.8	4943.2
50	13.5	150	-17	11.3	0.002378	260.4	2500.2	2882.2	5382.4
50	14	30	-14	12.0	0.000341	249.1	1213.5	476.5	1690.0
50	14	30	-20	12.0	0.000487	257.2	1435.1	793.2	2228.3
50	14	40	-8	12.2	0.00018	235.4	953.6	223.3	1176.8
50	14.5	30	-13	12.6	0.000279	244.7	1254.8	573.6	1824.8
50	9.5	30	-8	8.2	0.000196	237.2	334.5	5.2	339.7
50	9.5	40	-18	8.3	0.000559	260.4	563.0	8.0	571.0
55	10	50	-13	8.7	0.000458	255.8	590.6	8.5	599.1
55	10	50	-6	8.7	0.00016	232.9	367.9	5.6	373.5
55	10.5	150	-7	9.1	0.000504	258.0	725.5	11.5	737.0
55	10.5	80	-13	9.0	0.000718	266.3	826.8	13.3	840.1
55	10.5	90	-6	9.2	0.000225	240.1	504.2	7.4	511.6
55	11	100	-5	10.5	3.88E-05	208.0	346.0	6.1	351.9
55	11	60	-9	9.6	0.000329	248.4	679.9	15.3	695.2
55	11	70	-12	9.5	0.000551	260.1	856.2	24.1	880.3
55	11	90	-12	9.5	0.000695	265.5	952.7	30.4	983.0
55	11.5	10	-14	9.8	0.000121	227.1	462.6	8.7	471.1
55	11.5	10	-8	9.9	5.59E-05	212.8	349.0	5.6	354.5
55	11.5	20	-18	9.8	0.000298	246.2	688.5	21.5	710.0
55	11.5	30	-7	10.0	0.000117	226.4	477.1	10.5	487.6
55	11.5	40	-18	9.8	0.000549	260.0	928.1	48.1	976.2
55	12	30	-10	10.3	0.000209	238.5	681.7	37.0	718.7
55	12	80	-10	10.4	0.000476	256.7	1005.9	129.9	1135.7
55	12.5	10	-15	10.7	0.000125	227.9	593.9	31.0	625.0
55	12.5	100	-6	11.4	0.000103	223.9	656.3	52.9	709.2
55	12.5	20	-14	10.7	0.000217	239.3	768.4	69.4	837.7
55	12.5	20	-9	10.9	0.000115	226.1	597.1	34.6	631.3
55	12.5	60	-8	10.8	0.000253	242.6	839.5	101.6	941.1
55	12.5	90	-19	10.5	0.001397	270.7	1701.9	552.2	2254.1
55	13	10	-6	11.4	2.46E-05	202.2	359.6	10.2	369.2
55	13	100	-6	12.1	8.00E-05	218.9	662.2	63.2	724.6
55	13	20	-13	11.3	0.000184	235.8	804.5	105.8	910.4

55	13	30	-5	12.7	6.53E-06	186.9	304.0	15.8	314.8
55	13	50	-6	11.8	6.39E-05	214.6	568.2	36.8	604.4
55	13	50	-9	11.2	0.00027	244.0	946.6	168.3	1114.8
55	13	90	-10	11.3	0.000507	258.1	1264.5	438.1	1702.5
55	13	90	-8	11.3	0.000335	248.8	1073.9	263.7	1337.7
55	13.5	10	-7	11.7	3.92E-05	208.2	453.6	43.3	494.9
55	13.5	20	-10	11.7	0.000135	229.3	763.9	97.1	859.2
55	13.5	30	-20	11.5	0.000473	256.5	1267.9	470.7	1738.6
55	13.5	60	-12	11.7	0.000463	256.0	1306.7	545.2	1851.9
55	13.5	70	-20	11.5	0.001022	270.7	1802.0	1313.5	3115.4
55	14	30	-7	12.3	8.68E-05	220.5	720.6	85.9	802.2
55	14	70	-9	12.2	0.00033	248.4	1240.6	523.9	1764.4
60	10.5	10	-11	9.0	8.35E-05	219.7	311.6	4.7	316.4
60	10.5	50	-7	9.1	0.000184	235.8	451.5	6.7	458.2
60	10.5	90	-5	9.6	7.41E-05	217.4	354.9	5.1	360.0
60	11.5	30	-6	10.1	6.84E-05	215.9	395.2	7.4	402.5
60	11.5	50	-7	10.0	0.000163	233.3	557.4	16.0	573.3
60	11.5	60	-5	11.0	2.10E-05	200.2	312.7	10.1	319.0
60	12	40	-11	10.3	0.000277	244.6	775.3	55.3	830.6
60	12	40	-18	10.2	0.000507	258.1	998.5	100.2	1098.7
60	12	50	-15	10.3	0.000487	257.2	999.9	114.0	1113.9
60	12	60	-10	10.3	0.000352	249.9	868.0	76.7	944.6
60	12.5	40	-7	10.9	0.000121	227.2	613.9	37.5	650.6
60	12.5	50	-7	10.9	0.000142	230.4	667.5	50.4	717.9
60	12.5	60	-6	11.2	7.96E-05	218.8	556.9	29.6	586.0
60	13	100	-12	11.2	0.000698	265.6	1427.8	582.2	2009.9
60	13	30	-17	11.3	0.000312	247.2	1032.9	239.6	1272.5
60	13	40	-10	11.2	0.000241	241.6	896.9	139.2	1036.1
60	13.5	10	-20	11.5	0.000159	232.7	788.5	101.8	890.3
60	13.5	50	-10	11.7	0.000272	244.1	1069.1	282.6	1351.7
60	13.5	70	-13	11.7	0.000529	259.1	1413.6	668.2	2081.8
60	13.5	80	-11	11.6	0.000513	258.4	1351.3	576.3	1927.6
60	9.5	10	-11	8.2	8.27E-05	219.6	239.4	3.6	243.0
60	9.5	10	-14	8.3	0.000101	223.6	259.5	4.1	263.5
60	9.5	20	-10	8.2	0.000138	229.9	295.7	4.6	300.3

VITA

Daniel Angelo Boyd
Mechanical & Aerospace Engineering Department
238 Kaufman Hall
Norfolk, VA 23529

Professional Experience

Graduate Researcher - Aug 2016 to Aug 2018
Old Dominion University • NIA • NASA Langley Research Center Hampton Roads, VA

Graduate Teaching Assistant - Aug 2017 to Dec 2017
Old Dominion University Norfolk, VA.

Field Engineer - Nov 2015 to Jul 2016
Vincent Corporation Tampa, FL.

Artillery Officer - July 2008 to Dec 2014
United States Army Fort Hood and Bliss, TX; Iraq; Afghanistan

Education

Master of Science: Aerospace Engineering - Aug 2018
Old Dominion University Norfolk, VA.

Master of Arts: Management and Leadership - Aug 2015
Webster University St. Louis, MO.

Bachelor of Science: Mechanical Engineering with a Minor in Mathematics - May 2008
Virginia Military Institute Lexington, VA.